

A MULTI-FIDELITY PARAMETRIC FRAMEWORK FOR REDUCED-ORDER MODELING USING OPTIMAL TRANSPORT-BASED INTERPOLATION: APPLICATIONS TO DIFFUSED-INTERFACE TWO-PHASE FLOWS

MOAAD KHAMLICH¹, NICCOLÒ TONICELLO¹, FEDERICO PICHI¹, AND GIANLUIGI ROZZA¹

ABSTRACT. This work introduces a data-driven, non-intrusive reduced-order modeling (ROM) framework that leverages Optimal Transport (OT) for multi-fidelity and parametric problems. Building upon the success of displacement interpolation for data augmentation in handling nonlinear dynamics, we extend its application to more complex and practical scenarios. The framework is designed to correct a computationally inexpensive low-fidelity (LF) model to match an accurate high-fidelity (HF) one by capturing its temporal evolution via displacement interpolation while preserving the problem’s physical consistency. The framework is further extended to address systems dependent on a physical parameter, for which we construct a surrogate model using a hierarchical, two-level interpolation strategy. First, it creates synthetic HF checkpoints via displacement interpolation in the parameter space. Second, the residual between these synthetic HF checkpoints and a true LF solution is interpolated in the time domain using the multi-fidelity OT-based methodology. This strategy provides a robust and efficient way to explore the parameter space and to obtain a refined description of the dynamical system. The potential of the method is discussed in the context of complex and computationally expensive diffuse interface methods for two-phase flow simulations, which are characterized by moving interfaces and nonlinear evolution, and challenging to be dealt with traditional ROM techniques.

Keywords: Reduced-Order Models, Multi-Fidelity Modeling, Optimal Transport, Displacement Interpolation, Diffused-Interface, Allen-Cahn Equation, Data-Driven Modeling.

1. INTRODUCTION

Many engineering and scientific phenomena of practical interest can be accurately described by mathematical models based on partial differential equations (PDEs). The numerical solution of such PDEs is generally performed through spatio-temporal discretization, using methods like the Finite Element (FE) or Finite Volume (FV) methods, which transform the continuous problem into a system with a finite number N_h of degrees of freedom [56]. An accurate discretization of general PDEs often yields high-dimensional solution vectors, meaning that a proper description of their behavior requires a computationally intractable number of degrees of freedom ($N_h \gg 1$). For time-dependent problems, further discretization in time results in a sequence of large algebraic systems to be solved, compounding the computational burden.

Although these traditional high-fidelity (HF) models can provide robust and accurate predictions, their intrinsic computational cost often represents a bottleneck. This complexity has a substantial impact on their feasibility to analyze physical phenomena, especially when the HF strategy is part of a more general framework where its output serves as input for other tasks. In many practical scenarios, such as real-time control [41, 53], uncertainty quantification [6, 13], design optimization [10, 24], and inverse problems [34, 46], the computational demands of HF methods become prohibitive. The need to perform faster simulations, without excessively compromising their accuracy, has driven extensive research into the field of model order reduction [8, 28, 57].

Reduced-order models (ROMs) have emerged as a surrogate strategy exploiting data to alleviate the computational burden posed by accurate but costly HF methods, providing rapid and reliable evaluations. The key concept behind ROMs is that many practical problems exhibit dominant

¹ MATHLAB, MATHEMATICS AREA, SISSA, VIA BONOMEA 265, I-34136 TRIESTE, ITALY

patterns that can be described by a low-dimensional set of features. This allows to discard redundant variables in the description of the phenomena, motivating the use of dimensionality reduction techniques to compress the dataset constituted by physical simulation while retaining its essential properties. Typically, the construction of a ROM involves two main stages: an *offline stage*, where the computationally intensive work of generating high-fidelity solution snapshots and extracting dominant features occurs, and an *online stage*, where the pre-computed reduced representation is used to rapidly approximate the system’s solution for new parameter values or time instances. This offline-online decomposition makes ROMs particularly useful in the many-query and real-time settings.

A popular class of ROMs relies on projecting the governing equations onto a low-dimensional linear subspace, often constructed using Proper Orthogonal Decomposition (POD) [12, 67]. While effective for many diffusion-dominated problems [11, 39, 62], these linear-subspace methods encounter significant challenges when dealing with systems that exhibit strong nonlinearities or advection-dominated phenomena [5, 25, 29]. The mathematical root of this difficulty lies in the slow decay of the Kolmogorov n -width, which measures the degree of compactness of the solution manifold in terms of approximability by n -dimensional linear subspaces [15, 48, 50]. In particular, advection-dominated problems featuring steep gradients or traveling waves that move across the domain are very difficult to represent efficiently by linear methods with a fixed global basis. The moving nature of such features often leads to poor support intersection between snapshots at different time instances, fundamentally limiting the effectiveness of linear approximation and often resulting in Gibbs phenomena or requiring an impractically large reduced basis to maintain accuracy.

These fundamental limitations have spurred extensive research into more advanced ROM techniques. One direction involves adapting the data representation to better suit linear methods through shifted or registered POD approaches [9, 47, 70]. Another direction concerns the development of nonlinear reduction methodologies using deep learning frameworks [22, 40, 55], which seek to learn nonlinear mappings between the high-dimensional state space and a low-dimensional latent space.

In our previous work [38], we introduced a ROM framework that addresses these challenges by incorporating the concept of Displacement Interpolation (DI) from Optimal Transport (OT) theory [52, 64, 73] to enhance the representation of nonlinear dynamics in complex systems. OT, originally developed by Monge and Kantorovich, concerns the matching and transport of probability distributions by identifying the most cost-effective way to transform one into another. Unlike classical L^2 -based distance metrics that compare distributions pointwise, OT considers the “work” required to move a source mass distribution to match a target distribution, inherently accounting for the underlying geometry of the space. A fundamental concept in OT is the Wasserstein distance, which quantifies the minimum cost of transporting one distribution to another [7, 20, 21]. This distance defines a metric in the space of probability measures, endowing it with a Riemannian-like structure that allows for geometric operations such as the definition of geodesics and barycenters [1, 42]. The geometric perspective provided by OT is particularly attractive for ROMs concerned with the treatment of features that translate or deform, as the Wasserstein distance can capture these transformations in a more natural way compared to traditional Euclidean-based metrics. By interpreting solution snapshots as probability distributions and leveraging displacement interpolation—the construction of geodesic paths in Wasserstein space—our method generates physically plausible synthetic snapshots between sparse high-fidelity checkpoints, addressing the challenge of data scarcity while enabling continuous-time prediction [18, 33, 38].

In this paper, we extend this OT-based methodology to address two challenges in computational modeling that arise frequently in practice, namely the *multi-fidelity* and the *parametric* modeling.

Indeed, in the first context, the goal is to correct computationally inexpensive low-fidelity (LF) approximations with limited accuracy, for instance due to a coarser mesh or simplified physics, using information from a few expensive high-fidelity (HF) simulations [17, 30, 51]. Here, we propose a new approach where this information is retrieved by interpolating in time the residual field between HF and LF solutions via OT, leveraging the geometric structure of Wasserstein space to track the movement of discrepancy features.

Moreover, many physical systems depend on a set of parameters $\boldsymbol{\mu}$, such as material properties or boundary conditions, and the goal is to build a ROM capable of rapid prediction for any $\boldsymbol{\mu}$ within a given parameter domain. To investigate efficiently different system's configurations, we introduce a hierarchical, two-level interpolation strategy to simultaneously deal with both parameter and time dependency. In the first level, we use the OT-based displacement interpolation across the parameter space to generate synthetic HF snapshots for unseen parameter value from HF checkpoints computed at nearby training points. In the second level, we compute the residual between these physically consistent HF synthetic data and true LF simulations at the test parameter, and then apply our multi-fidelity framework to interpolate this residual in time. This approach avoids the construction of a monolithic ROM over the joint time-parameter space, which can be prohibitively complex. These two extensions, the Multi-Fidelity OT-ROM (MF-OT-ROM) and the Parametric Multi-Fidelity OT-ROM (PMF-OT-ROM), broaden the applicability of our original method.

We frame our discussion within the context of two-phase flow modelling using the conservative Allen-Cahn equation [14]. More broadly, diffuse-interface methods have gained significant attention in the computational fluid dynamics community due to their versatility across different numerical schemes, governing equations, and flow regimes (incompressible or compressible, laminar or turbulent), as well as their relative ease of implementation [65]. The widespread adoption of these approaches has enabled the simulation of highly complex two-phase flows, which are often characterized by strongly coupled phenomena, including interfacial mass and heat transfer [44], phase change [63], boiling [32, 60, 74], turbulence [61, 68], and strong compressibility effects [16, 31, 71], among others. These capabilities make diffuse-interface methods particularly suitable for tackling multi-physics scenarios that are challenging to address with sharp-interface models.

In particular, recent developments of the conservative Allen-Cahn equation and its variants have yielded numerical methods with several desirable properties, including enhanced mass conservation [69], strict boundedness [43], and efficient interface sharpening [2, 35]. Despite the growing literature on high-fidelity simulations employing these methodologies, the integration of reduced-order modelling strategies remains largely unexplored in this field. Two-phase flows fall into the broader category of advection-dominated problems, for which classical linear ROMs often struggle to maintain accuracy and robustness, especially in the presence of complex interfacial dynamics and multi-scale interactions.

In this work, we extend the methodological developments of OT-based ROMs and investigate their applicability to two-phase flow simulations. By doing so, we aim to bridge the gap between high-fidelity diffuse-interface models and computationally efficient ROMs, providing new avenues for reduced-order modelling in a challenging and highly relevant class of multi-physics problems.

The remainder of the paper is structured as follows. Section 2 provides the necessary mathematical background on reduced-order modeling and optimal transport theory, and summarizes the core OT-ROM methodology from our previous work [38], which serves as the foundation for the extensions presented here. Section 3 introduces multi-fidelity residual interpolation, while Section 4 presents parametric displacement interpolation, applicable to both single- and multi-fidelity settings. Section 5 introduces the conservative Allen-Cahn equation coupled within the five-equation model, while Section 6 is reserved for numerical experiments. Finally, Section 7 provides concluding remarks and directions for future research.

2. PRELIMINARIES

We consider time-dependent PDE problems defined on a spatial domain $\Omega \subset \mathbb{R}^d$ over a time interval $\mathcal{I} = [0, t_f]$. After spatial discretization using, for instance, FE or FV methods, the state of the system at time t is represented by a vector $\mathbf{u}(t) \in \mathbb{R}^{N_h}$, where N_h denotes the number of degrees of freedom. Given a fixed parametric configuration, the collection of solutions over time traces out a solution manifold $\mathcal{M} = \{\mathbf{u}(t) \mid t \in \mathcal{I}\}$ embedded in the high-dimensional space \mathbb{R}^{N_h} . In practice, we work with a discrete set of N_T snapshots collected at times $\{t_k\}_{k=1}^{N_T}$, which we arrange into the snapshot matrix $\mathbf{S} = [\mathbf{u}(t_1) \mid \mathbf{u}(t_2) \mid \dots \mid \mathbf{u}(t_{N_T})] \in \mathbb{R}^{N_h \times N_T}$.

2.1. Reduced-Order Modeling: The Offline-Online Paradigm. ROM emerged as class of surrogate strategies to alleviate computational bottlenecks posed by HF methods [8, 28, 57].

In particular, dimensionality reduction techniques aim to identify the underlying low-dimensional structure of the dominant pattern of the solution manifold characterized by the evolution in time and the variation w.r.t. input parameters. Toward this goal, the system dynamics is projected onto this reduced set of coordinates, building a surrogate model that is much faster to solve than its HF counterpart, and retain the essential physical characteristics and accuracy.

The construction of a ROM typically involves two main stages. In the *offline stage*, which is computationally intensive and can exploit high-performance computing resources, one generates a set of high-fidelity solutions (snapshots) for several values of the parameter or time instances. These snapshots are processed to extract the main modes that describe the system’s behavior, and a low-dimensional basis is constructed to represent the system’s dynamics in the reduced space. In the *online stage*, the pre-computed reduced representation is used to rapidly approximate the system’s solution for new parameter values or time instances. Since the computations occur in a significantly smaller dimensional space ($N_r \ll N_h$), this stage entails extremely fast evaluation.

The so-called projection-based ROMs approximate the high-dimensional solution $\mathbf{u}(t)$ as the linear combination of a few basis functions:

$$\mathbf{u}(t) \approx \mathbf{V}\mathbf{a}_r(t), \quad (1)$$

where $\mathbf{V} \in \mathbb{R}^{N_h \times N_r}$ is a matrix whose $N_r \ll N_h$ orthonormal columns span a low-dimensional subspace, and $\mathbf{a}_r(t) \in \mathbb{R}^{N_r}$ contains the reduced coordinates. A common choice for \mathbf{V} is the POD basis, obtained by computing the singular value decomposition (SVD) of the snapshot matrix:

$$\mathbf{S} = \mathbf{U}\mathbf{\Sigma}\mathbf{W}^T, \quad (2)$$

where $\mathbf{U} \in \mathbb{R}^{N_h \times N_T}$ contains the left singular vectors (POD modes), $\mathbf{\Sigma}$ is a diagonal matrix of singular values $\sigma_1 \geq \sigma_2 \geq \dots \geq \sigma_{N_T} \geq 0$, and \mathbf{W} contains the right singular vectors. The reduced basis \mathbf{V} is formed by retaining only the first N_r columns of \mathbf{U} , corresponding to the largest singular values. The truncation is typically chosen to capture a prescribed fraction of the total energy:

$$\frac{\sum_{i=1}^{N_r} \sigma_i^2}{\sum_{i=1}^{N_T} \sigma_i^2} \geq 1 - \epsilon, \quad (3)$$

where ϵ is a small tolerance. The rate at which the singular values decay determines how many modes are needed for an accurate approximation, and thus the reliability of the ROM ansatz. As described by the Kolmogorov n -width decay analysis [15, 48, 50], for advection-dominated problems with moving features this decay is typically slow, necessitating a large number of modes and diminishing the computational advantage of the ROM.

2.2. Optimal Transport and Displacement Interpolation. Optimal Transport (OT) theory provides a geometric framework for comparing and morphing probability distributions [52, 73]. At its core, OT addresses the problem of finding the most efficient way to transform one distribution of mass into another, where efficiency is measured by a total transportation cost. The theory was originally posed by Monge, looking for the cheapest way to transport soil to fill a hole [45], and later relaxed by Kantorovich [37] allowing mass from a single source point to be split and distributed among multiple destinations, leading to the modern theory of finding transport maps, for a given cost, which are optimal in matching source and target distributions. Figure 1 illustrates the difference between the two formulations in terms of mass splitting and the resulting transport plans.

We specialize directly to the discrete setting, which is of practical importance for numerical applications. Let the source and target measures be discrete probability measures with finite supports, written as weighted sums of Dirac masses:

$$\mu = \sum_{i=1}^n a_i \delta_{\mathbf{x}_i}, \quad \text{with } \mathbf{a} \in \mathbb{R}_+^n, \quad \sum_{i=1}^n a_i = 1, \quad (4)$$

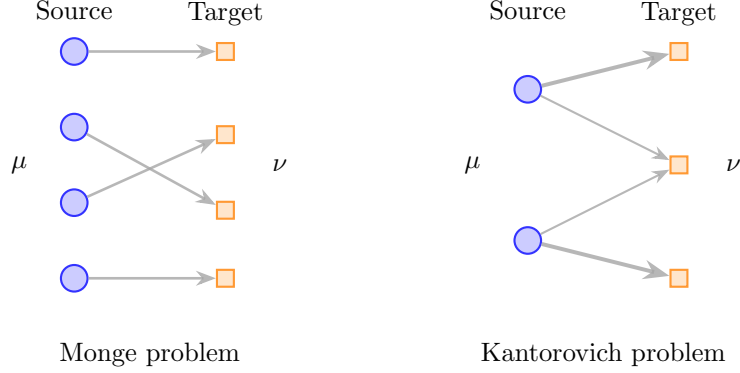


FIGURE 1. Illustration of the different OT problem formulations, depicting the mass transport plan π_{ij} proportional to the thickness of the arrows.

$$\nu = \sum_{j=1}^m b_j \delta_{\mathbf{y}_j}, \quad \text{with } \mathbf{b} \in \mathbb{R}_+^m, \quad \sum_{j=1}^m b_j = 1, \quad (5)$$

where $\mathbf{a} = (a_1, \dots, a_n)^T$ and $\mathbf{b} = (b_1, \dots, b_m)^T$ are the weight vectors (or histograms) of the measures. A *coupling* or *transport plan* between μ and ν is represented by a matrix $\boldsymbol{\pi} \in \mathbb{R}_+^{n \times m}$, where π_{ij} specifies how much mass is transported from \mathbf{x}_i to \mathbf{y}_j . The set of admissible couplings is the convex polytope of matrices with the prescribed marginals:

$$\Pi(\mu, \nu) = \{ \boldsymbol{\pi} \in \mathbb{R}_+^{n \times m} \mid \boldsymbol{\pi} \mathbf{1}_m = \mathbf{a}, \boldsymbol{\pi}^T \mathbf{1}_n = \mathbf{b} \}, \quad (6)$$

where $\mathbf{1}_k$ denotes a vector of ones of size k . The cost function $c(\mathbf{x}, \mathbf{y})$, representing the cost of moving a unit of mass from \mathbf{x} to \mathbf{y} , is encoded in a cost matrix $\mathbf{C} \in \mathbb{R}^{n \times m}$ with $C_{ij} = c(\mathbf{x}_i, \mathbf{y}_j)$.

The Kantorovich problem of finding the optimal (cheapest) transport plan then becomes the following linear program:

$$C(\mu, \nu) = \min_{\boldsymbol{\pi} \in \Pi(\mu, \nu)} \sum_{i=1}^n \sum_{j=1}^m C_{ij} \pi_{ij} = \min_{\boldsymbol{\pi} \in \Pi(\mu, \nu)} \langle \mathbf{C}, \boldsymbol{\pi} \rangle_F, \quad (7)$$

where $\langle \cdot, \cdot \rangle_F$ denotes the Frobenius inner product.

When the cost function is the p -th power of the Euclidean distance, the p -th root of the optimal cost defines the p -Wasserstein distance:

$$W_p(\mu, \nu) = \left(\min_{\boldsymbol{\pi} \in \Pi(\mu, \nu)} \sum_{i,j} \|\mathbf{x}_i - \mathbf{y}_j\|^p \pi_{ij} \right)^{1/p}. \quad (8)$$

The space of probability measures equipped with this metric inherits a rich geometric structure. Unlike classical L^2 -based metrics, which only measure pointwise differences, the Wasserstein distance is sensitive to the spatial displacement of features. Two distributions representing a feature and its translated counterpart are close in Wasserstein distance, reflecting the physical intuition that small translations should correspond to small distances. Then, it is clear that the choice of the underlying metric is particularly relevant in the context of physical fields exhibiting sharp contrasts, discontinuous features and small compact supports.

A fundamental property of spaces endowed with the Wasserstein metric is that they admit geodesics, i.e., shortest paths between measures. Given an optimal transport plan $\boldsymbol{\pi}^*$ between μ_0 and μ_1 , one can construct a geodesic path $\{\mu_t\}_{t \in [0,1]}$ called the *displacement interpolation* or McCann interpolation:

$$\mu_t = \sum_{i=1}^n \sum_{j=1}^m \pi_{ij}^* \delta_{(1-t)\mathbf{x}_i + t\mathbf{y}_j}, \quad (9)$$

where each mass π_{ij}^* travels along a straight line from source point \mathbf{x}_i to target point \mathbf{y}_j , with its position at time t given by the convex combination $(1-t)\mathbf{x}_i + t\mathbf{y}_j$. This path is a constant-speed geodesic satisfying:

$$W_p(\mu_s, \mu_t) = |t - s| W_p(\mu_0, \mu_1), \quad \forall s, t \in [0, 1]. \quad (10)$$

The displacement interpolation provides a geometrically natural way to “morph” between distributions, and given its nice properties in dealing with moving features, we leverage this as the key tool for generating synthetic snapshots describing the time- and parametric-evolution of physical fields.

The classical OT problem can be computationally expensive to solve due to its stiffness, particularly for large-scale problems. Entropic regularization [19] addresses this by adding a strictly convex penalty term based on the Kullback-Leibler (KL) divergence, ensuring that the problem has a unique minimizer. The regularized OT problem can be formulated as:

$$C_\epsilon(\mu, \nu) = \min_{\pi \in \Pi(\mu, \nu)} \{ \langle \mathbf{C}, \boldsymbol{\pi} \rangle_F + \epsilon \text{KL}(\boldsymbol{\pi} \| \mathbf{a}\mathbf{b}^T) \}, \quad (11)$$

where the KL divergence for discrete measures used as penalty term is given by:

$$\text{KL}(\boldsymbol{\pi} \| \mathbf{a}\mathbf{b}^T) = \sum_{i,j} \pi_{ij} \log \left(\frac{\pi_{ij}}{a_i b_j} \right). \quad (12)$$

In Equation (11), the regularization parameter $\epsilon > 0$ controls the trade-off between fidelity to the original OT problem (small ϵ) and computational efficiency (large ϵ). The effect of ϵ on the transport plan defined by the unique minimizer $\boldsymbol{\pi}_\epsilon$ is illustrated in Figure 2: for small ϵ , the plan is sharp and concentrated along the optimal paths, while for larger ϵ , it becomes increasingly diffuse, spreading mass more uniformly.

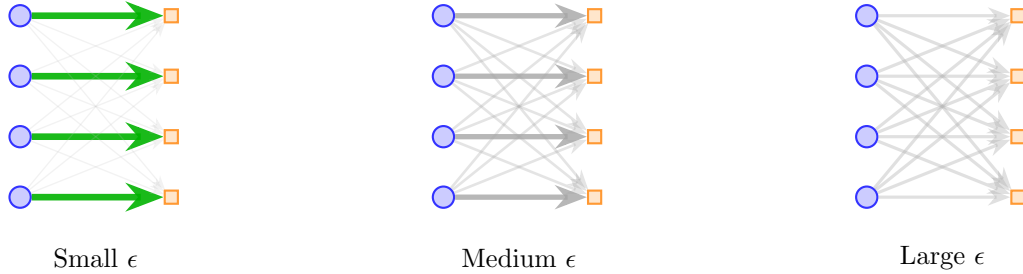


FIGURE 2. Effect of the entropic regularization increasing the parameter ϵ , from left to right the plan becomes smoother and more diffuse.

The main advantage of considering the regularized problem is that, exploiting results on the duality of linear minimization problems and the definitions of Kantorovich potentials [73], it admits a solution for which the optimal plan has the following simple multiplicative structure

$$\boldsymbol{\pi}_\epsilon = \text{diag}(\mathbf{u}) \mathbf{K} \text{diag}(\mathbf{v}), \quad \text{or component-wise, } (\boldsymbol{\pi}_\epsilon)_{ij} = u_i K_{ij} v_j, \quad (13)$$

where the Gibbs kernel is defined as:

$$\mathbf{K} = \exp(-\mathbf{C}/\epsilon), \quad \text{i.e., } K_{ij} = e^{-C_{ij}/\epsilon}, \quad (14)$$

and $\mathbf{u} \in \mathbb{R}_+^n$ and $\mathbf{v} \in \mathbb{R}_+^m$ are scaling vectors, that can be computed efficiently via the Sinkhorn algorithm [66]. Starting from the initial vector $\mathbf{v}^{(0)} = \mathbf{1}_m$, this iterative fixed-point procedure alternates between row and column normalizations:

$$\mathbf{u}^{(\ell+1)} = \mathbf{a} \oslash (\mathbf{K}\mathbf{v}^{(\ell)}), \quad \mathbf{v}^{(\ell+1)} = \mathbf{b} \oslash (\mathbf{K}^T \mathbf{u}^{(\ell+1)}), \quad (15)$$

where \oslash denotes element-wise division, and converges to the unique scaling vectors satisfying the marginal constraints. We remark that the algorithm consists entirely of matrix-vector products, making it highly parallelizable and well-suited for GPU acceleration.

Displacement interpolation extends naturally to the entropy-regularized setting by replacing the optimal plan π^* with its regularized counterpart π_ϵ in (9):

$$\mu_t^{(\epsilon)} = \sum_{i=1}^n \sum_{j=1}^m (\pi_\epsilon)_{ij} \delta_{(1-t)\mathbf{x}_i + t\mathbf{y}_j}. \quad (16)$$

The concept also generalizes to multiple measures via Wasserstein barycenters. Given measures $\{\mu_k\}_{k=1}^K$ with weights $\{\lambda_k\}$ summing to 1, the barycenter $\bar{\mu}$ minimizes:

$$\bar{\mu} = \arg \min_{\mu \in \mathcal{P}_2(\mathbb{R}^d)} \sum_{k=1}^K \lambda_k W_2^2(\mu, \mu_k). \quad (17)$$

This provides a geometrically meaningful ‘‘average’’ of distributions and can be used for multi-source parametric interpolation when more than two training parameters are involved.

A critical requirement for applying OT is that the fields to be interpolated must be non-negative, as they are interpreted as probability mass distributions. Solution fields that are inherently non-negative, such as densities or concentrations, can be directly normalized to have unit mass. For fields containing both positive and negative values, such as general physical fields or residuals, a simple decomposition into positive and negative parts can be applied, with each part interpolated separately.

2.3. OT-Based Displacement Interpolation for ROM. In this final section, we summarize the core OT-ROM methodology introduced in our previous work [38], which serves as the foundation for the extensions presented in this paper. The central idea is to use displacement interpolation to generate synthetic snapshots between sparse high-fidelity checkpoints, addressing data scarcity in ROM construction.

Consider a time-dependent problem whose solution $\mathbf{u}(t)$ is available at a sparse set of N_c checkpoint times $\{t_k\}_{k=1}^{N_c}$. The goal is to construct a continuous-in-time approximation $\mathbf{u}_{\text{synth}}(t)$ for any $t \in [t_1, t_{N_c}]$ via the displacement interpolation framework. The procedure, allowing for the efficient evaluation of time-trajectory snapshots and data-augmentation tasks, is structured as follows:

- (1) **Offline Stage: computation of the optimal transport plans**
 - (a) For each checkpoint, normalize the field $\mathbf{u}(t_k)$ by its mass $m_k = \|\mathbf{u}(t_k)\|_{L^1(\Omega)}$ to obtain a probability measure.
 - (b) For each consecutive pair of checkpoints (t_k, t_{k+1}) , compute the entropic OT plan π_ϵ^k between the normalized fields using the Sinkhorn algorithm.
- (2) **Online Stage: prediction at time t^***
 - (a) For a query time $t^* \in [t_k, t_{k+1}]$, compute the local interpolation parameter playing the role of ‘‘virtual time’’ defined by $\alpha = (t^* - t_k)/(t_{k+1} - t_k)$.
 - (b) Interpolate the mass via $m(\alpha) = (1 - \alpha)m_k + \alpha m_{k+1}$.
 - (c) Apply displacement interpolation using the pre-computed plan π_ϵ^k :

$$\mathbf{u}_{\text{synth}}(\alpha) = m(\alpha) \sum_{\ell, m} (\pi_\epsilon^k)_{\ell m} \delta_{\text{proj}_{\mathcal{X}}((1-\alpha)x_\ell + \alpha x_m)}, \quad (18)$$

where $\mathcal{X} = \{x_\ell\}_{\ell=1}^{N_h}$ denotes the discretization points and $\text{proj}_{\mathcal{X}}(\cdot)$ maps each point to its nearest grid location.

This approach exploits the geometric structure of Wasserstein space to transport features between their positions at time t_k and t_{k+1} , rather than simply blending them pointwise as in linear interpolation, which would be completely ineffective in the case of moving features with compact support. Moreover, the resulting synthetic snapshots preserve mass and follow geodesic paths in the space of probability measures, and thus, despite being a data-driven approach, this promotes physical and geometric consistency with the underlying PDEs.

Remark 2.1. *Instead of choosing the standard linear time mapping for the virtual time α , one could also consider the more accurate nonlinear time mapping introduced in [38], which minimizes the L^2 error between synthetic and true snapshots. In general, accounting for multi-scale behavior in time*

could prove crucial for the accuracy of the online reconstruction, but for the problems considered here the linear mapping has been sufficient to provide accurate results.

Remark 2.2. We remark that the accuracy of the OT-based interpolation can be further enhanced by a POD-based correction step [38]. This involves constructing a POD basis for the dominant error modes and using Gaussian Process Regression to predict correction coefficients. To be able to assess the effectiveness of the plain displacement interpolation approach in the context of two-phase flows, we do not employ the correction in the present work.

3. MULTI-FIDELITY RESIDUAL INTERPOLATION

In many applications, one has access to models of varying fidelity, which could originate from different assumptions or discretization. A high-fidelity model provides accurate solutions $\mathbf{u}_{\text{HF}}(t)$ but at substantial computational cost, while a low-fidelity solution $\mathbf{u}_{\text{LF}}(t)$ can be evaluated cheaply but with reduced accuracy. In particular, the LF model might arise from a coarser spatial discretization, a larger time step, or simplified physics. The goal of multi-fidelity modeling is to combine the strengths of both: exploiting the efficiency of LF models to obtain many simulation data to complete the missing information obtained from a limited number of HF simulations [51]. In practice, this strategy allows for an efficient exploration of the solution manifold, both in the offline and in the online phases, exploiting a cheaper model to generate many snapshots and building a non-intrusive real-time surrogate, respectively.

A straightforward strategy is to model the residual or discrepancy field $\mathbf{r}(t) = \mathbf{u}_{\text{HF}}(t) - \mathbf{u}_{\text{LF}}(t)$, which captures the difference between the two models. The HF solution can then be approximated as $\mathbf{u}_{\text{HF}}(t) \approx \mathbf{u}_{\text{LF}}(t) + \mathbf{r}_{\text{approx}}(t)$, where $\mathbf{r}_{\text{approx}}(t)$ is a reduced-order and efficient-to-evaluate representation of the residual. In standard multi-fidelity ROMs, one constructs a POD basis from residual snapshots and uses regression techniques to predict the reduced coefficients at new time instances. However, for problems with moving features, the residual field itself exhibits advective dynamics that are poorly captured by linear interpolation in the POD coefficient space, motivating our OT-based approach.

We propose to use displacement interpolation to model the temporal evolution of the residual field, developing the Multi-Fidelity OT-ROM (MF-OT-ROM) strategy illustrated in Figure 3. Given HF and LF snapshots at checkpoint times $\{t_k\}_{k=1}^{N_c}$, we compute residual checkpoints $\mathbf{r}_k = \mathbf{u}_{\text{HF}}(t_k) - \mathbf{u}_{\text{LF}}(t_k)$ and apply OT-based interpolation to generate $\mathbf{r}_{\text{interp}}(t^*)$ for any query time t^* . Since residual fields typically contain both positive and negative values, we apply a simple decomposition into positive and negative parts, $\mathbf{r} = \mathbf{r}^+ - \mathbf{r}^-$, with each part interpolated separately before recombination, so that the final multi-fidelity approximation is given by

$$\mathbf{u}_{\text{approx}}(t^*) = \mathbf{u}_{\text{LF}}(t^*) + \mathbf{r}_{\text{interp}}(t^*). \quad (19)$$

This multi-fidelity approach offers clear advantages over simply applying standard interpolation (e.g., linear or spline) to residual coefficients in a POD basis, especially in this context. Indeed, the OT-based interpolation inherently respects the geometric structure and movement of features within the residual field, and thus, for phase-field problems, where the residual is often concentrated at the moving interface, the method can effectively “transport” the correction from its position at

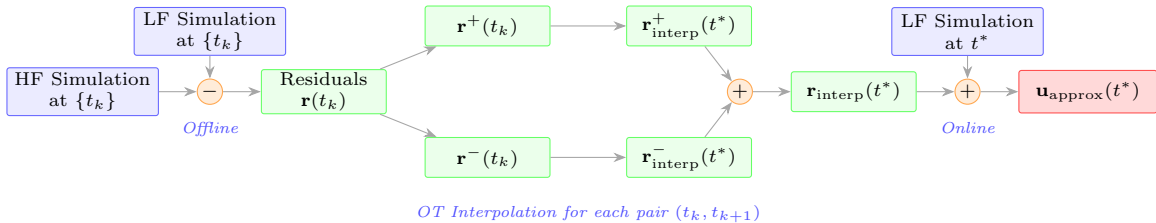


FIGURE 3. Schematic of the multi-fidelity OT-ROM framework, using displacement interpolation on the residual between HF and LF models.

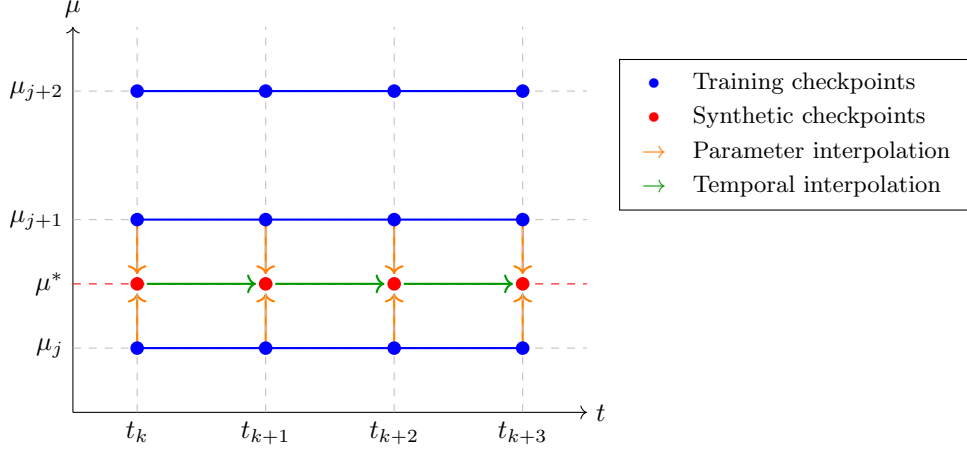


FIGURE 4. Parametric and temporal displacement interpolation on the (t, μ) grid.

t_k to its new position at t_{k+1} , rather than just fading out the old correction and fading in the new one.

4. PARAMETRIC DISPLACEMENT INTERPOLATION

In the previous sections, we have specifically considered time-dependent problems as the natural framework where to exploit our strategy. Nevertheless, being a data-driven strategy, both temporal or parametric nature of the moving features can be treated in a similar way, thus we are interested in extending the strategy proposed in [38] to perform displacement interpolation for problems with parametric dependencies. More specifically, in the formulation presented so far, time t serves as the interpolation coordinate in the solution manifold, with OT plans computed between consecutive temporal checkpoints, while we aim at including additional parameters $\mu \in \mathcal{P} \subset \mathbb{R}^p$, modeling physical characteristics of the systems, such as material properties and boundary conditions, or geometric properties.

In Figure 4, we present the procedure to exploit a dataset of dynamical systems corresponding to different parameter values performing a two-stage displacement interpolation strategy to obtain synthetic checkpoints for newly given parameters and recover their temporal evolution. Practically speaking, given solution snapshots at training parameter values $\{\mu_j\}_{j=1}^{N_p}$ and checkpoint times $\{t_k\}_{k=1}^{N_c}$, we can interpolate along both coordinate directions: temporally at fixed parameter, or parametrically at fixed time. For a test parameter $\mu^* \in (\mu_j, \mu_{j+1})$, OT plans are computed between snapshots at adjacent training parameters for each checkpoint, and synthetic checkpoints are generated via parametric displacement interpolation with factor $\alpha_\mu = (\mu^* - \mu_j) / (\mu_{j+1} - \mu_j)$. Finally, temporal displacement interpolation is exploited to connect these and obtain efficient and reliable predictions for any query time. The extension to higher-dimensional parameter spaces can be done in several ways, exploiting additional knowledge on the parametric dependency, considering tensor product of grids, or using Wasserstein barycenters. Since all these extensions could potentially require a dramatic increase of the computational cost when the number of parameters increases, we postpone the investigation of an efficient strategy to following works.

Finally, we introduce the Parametric Multi-Fidelity OT-ROM (PMF-OT-ROM), combining the multi-fidelity framework from Section 3 with the parametric setting. We start by noticing that two strategies are possible, depending on the field being considered. The first approach entails applying parametric displacement interpolation directly to the HF training data to generate synthetic HF checkpoints $\mathbf{u}_{\text{HF}}^{\text{synth}}(t_k; \mu^*)$. A cheap LF simulation is run at μ^* , and the synthetic residuals $\mathbf{r}^{\text{synth}}(t_k) = \mathbf{u}_{\text{HF}}^{\text{synth}}(t_k) - \mathbf{u}_{\text{LF}}(t_k)$ are interpolated in time to produce the final approximation $\mathbf{u}_{\text{approx}}(t) = \mathbf{u}_{\text{LF}}(t) + \mathbf{r}_{\text{interp}}(t)$.

On the other hand, the second strategy computes residuals at each training parameter value, then applies parametric displacement interpolation to these residual fields to generate synthetic residual checkpoints $\mathbf{r}^{\text{synth}}(t_k; \mu^*)$. Both strategies avoid constructing a monolithic ROM over the joint (t, μ) space, rather they explore the displacement interpolation along the two coordinates shifting the focus from the physical to the residual fields. The former approach is conceptually simpler, especially for applications where the high-fidelity solution has relevant physical meaning, while residual interpolation could be less intuitive, but preserving the same characteristics of moving features, it may be advantageous when its behavior with respect to μ varies more smoothly than the full solution.

Finally, we remark that a key assumption is that the solution (or the residual) evolves smoothly with μ , thus problems exhibiting bifurcations [27, 54] or sharp transitions in parameter space [29, 59], more sophisticated strategies such as local model order reduction [4, 23] or adaptive sampling [36, 49] may be required.

5. PROBLEM DEFINITION: FIVE EQUATION MODEL

The proposed methodological extension of OT-based ROMs are applied in this work to the simulation of compressible two-phase flows. Specifically, the full-order model relies on the five-equation formulation originally introduced by Allaire et al. [3]. Compared to the original model, the present approach incorporates an additional transport equation for the level-set function ψ , which is employed to evaluate the interface normal vectors, following a strategy similar to that proposed by Al-Salami et al. [2].

The five-equation model reads:

$$\frac{\partial \psi}{\partial t} + \mathbf{u} \cdot \nabla \psi = 0, \quad (20)$$

$$\frac{\partial \phi_l}{\partial t} + \mathbf{u} \cdot \nabla \phi_l = \nabla \cdot \mathbf{a}_l, \quad (21)$$

$$\frac{\partial(\rho_l \phi_l)}{\partial t} + \nabla \cdot (\rho_l \phi_l \mathbf{u}) = \nabla \cdot \mathbf{R}_l, \quad l = \{1, 2\}, \quad (22)$$

$$\frac{\partial(\rho \mathbf{u})}{\partial t} + \nabla \cdot (\rho \mathbf{u} \otimes \mathbf{u} + p \mathbb{I}) = \nabla \cdot (\mathbf{f} \otimes \mathbf{u}) + \nabla \cdot \boldsymbol{\tau} + \sigma \kappa \nabla \phi_1, \quad (23)$$

$$\begin{aligned} \frac{\partial(\rho E)}{\partial t} + \nabla \cdot [(\rho E + p) \mathbf{u}] &= \nabla \cdot (\mathbf{f} g) + \sum_{l=1}^2 \nabla \cdot (\rho_l H_l \mathbf{a}_l) \\ &+ \nabla \cdot (\boldsymbol{\tau} \cdot \mathbf{u}) + \sigma \kappa \nabla \phi_1 \cdot \mathbf{u}, \end{aligned} \quad (24)$$

where ϕ_l denotes the l^{th} phase field and H_l its specific enthalpy. The variable ρ is the mixture density, $\rho \mathbf{u}$ the total momentum, and p the pressure. The total energy is defined as $\rho E = \rho e + \frac{1}{2} \rho \|\mathbf{u}\|^2$, i.e., the sum of internal and kinetic energy. The parameter σ denotes the surface tension coefficient and $\kappa = -\nabla \cdot \hat{\mathbf{n}}_1$ the interface curvature.

The following auxiliary quantities have been introduced:

$$\mathbf{a}_l = \Gamma [\varepsilon \nabla \phi_l - \phi_l (1 - \phi_l) \hat{\mathbf{n}}_l], \quad \hat{\mathbf{n}}_l = \frac{\nabla \psi}{\|\nabla \psi\|}, \quad (25)$$

$$\mathbf{R}_l = \rho_l^{(0)} \mathbf{a}_l, \quad \mathbf{f} = \sum_{l=1}^2 \mathbf{R}_l, \quad g = \frac{1}{2} \|\mathbf{u}\|^2. \quad (26)$$

The parameters ε and Γ characterize the Allen-Cahn regularization. In particular, ε controls the interface thickness and is typically chosen proportional to the grid size, while Γ regulates the magnitude of the regularization relative to advection and is commonly scaled with the maximum velocity magnitude in the computational domain.

The viscous stress tensor is defined as

$$\boldsymbol{\tau} = 2\mu \left(\mathbb{S} - \frac{1}{3} (\nabla \cdot \mathbf{u}) \mathbb{I} \right),$$

where μ is the mixture dynamic viscosity, evaluated as $\mu = \mu_1\phi_1 + \mu_2\phi_2$, and $\mathbb{S} = [\nabla\mathbf{u} + (\nabla\mathbf{u})^\top]/2$ denotes the strain-rate tensor.

The system is closed by relating the internal energy to the pressure through a stiffened-gas equation of state (EOS) [26]:

$$p = \frac{\rho e - \left(\frac{\gamma_1 p_1^\infty}{\gamma_1 - 1} \phi_1 + \frac{\gamma_2 p_2^\infty}{\gamma_2 - 1} \phi_2 \right)}{\left(\frac{\phi_1}{\gamma_1 - 1} + \frac{\phi_2}{\gamma_2 - 1} \right)}, \quad (27)$$

where γ_l and p_l^∞ are the EOS parameters of the l^{th} phase. The corresponding speed of sound and specific enthalpy for each phase are given by

$$c_l = \sqrt{\gamma_l \left(\frac{p + p_l^\infty}{\rho_l} \right)} \quad \text{and} \quad H_l = \frac{(p + p_l^\infty)\gamma_l}{\rho_l(\gamma_l - 1)}, \quad l = \{1, 2\}. \quad (28)$$

For completeness, the following mixture relations hold:

$$\phi_2 = 1 - \phi_1, \quad (29)$$

$$\rho = \rho_1\phi_1 + \rho_2\phi_2, \quad (30)$$

$$\frac{1}{\gamma - 1} = \phi_1 \frac{1}{\gamma_1 - 1} + \phi_2 \frac{1}{\gamma_2 - 1}, \quad (31)$$

$$p^\infty \frac{\gamma}{\gamma - 1} = \phi_1 \frac{\gamma_1 p_1^\infty}{\gamma_1 - 1} + \phi_2 \frac{\gamma_2 p_2^\infty}{\gamma_2 - 1}. \quad (32)$$

In the following section, we introduce the numerical benchmarks employed to assess the OT-based methodologies. The spatial discretization of the five-equation model, in both kinetic and fully coupled configurations, is performed using a high-order Spectral Difference scheme (see [72] for further details regarding the numerical discretization of the five equation model).

In kinetic tests, the phase field evolves under a prescribed analytical velocity field, whereas in the fully coupled configuration the complete system of governing equations is solved. As representative kinetic benchmark, we consider the Rider-Kothe vortex, while the Rayleigh-Taylor instability is adopted as the fully coupled test case. Both problems are inherently unsteady and involve explicit parametric dependencies in their initial conditions.

In all cases, the analysis focuses on the accurate prediction of interfacial dynamics. The primary quantity of interest is the phase-field variable ϕ_1 . Although the same framework can be extended to other flow variables with different physical interpretations, ϕ_1 is selected due to its central role in the modeling of two-phase compressible flows.

6. NUMERICAL RESULTS

In this section, we assess the performance of the proposed MF-OT-ROM and PMF-OT-ROM frameworks on benchmark problems based on the five equation model described in Section 5. In order to present a comprehensive evaluation of the performance of both frameworks, for the MF-OT-ROM, we demonstrate the accuracy of the residual interpolation and the improvement over the standalone LF model, while for the PMF-OT-ROM, we evaluate the model's ability to predict solutions for unseen parameter values.

6.1. Rider-Kothe vortex. A classical test case for interface capturing techniques consists in the deformation of a two-dimensional circular bubble by a shear flow [58]. In particular, in the classical test, a droplet of radius $R = 0.15$ centered at $(0.0, 0.25)$ in a $[-0.5, 0.5]^2$ square periodic domain is advected by the following divergence-free velocity field:

$$\begin{bmatrix} u_1 \\ u_2 \end{bmatrix} = \begin{bmatrix} \sin^2(\pi(x_1 + 0.5)) \sin(2\pi(x_2 + 0.5)) \cos\left(\frac{\pi t}{T}\right) \\ -\sin(2\pi(x_1 + 0.5)) \sin^2(\pi(x_2 + 0.5)) \cos\left(\frac{\pi t}{T}\right) \end{bmatrix}, \quad (33)$$

where T denotes the characteristic period of the shear flow, which we have chose as the classical value $T = 4$ for this particular test. Under the action of such a velocity field, in the first half of the period, the initial circular bubble is strongly deformed into a thin filament. After velocity reversal, the

filament is stretched back to the initial condition. It is already clear that this benchmark possesses several challenges from both the high-fidelity and reduced-order modeling perspectives. Indeed, the strong deformation of the interface leading to sharp and very localized features, the advection-dominated nature of the problem with significant variations of its support, and the complexity of the nonlinear dynamics, all contribute to making this physical phenomena a very challenging test case to verify the capabilities of our strategies in accurately predicting the phase field.

Thus, given the highly refined grid needed to capture the sharp and thin features of the interface, and the notable differences between snapshots at different time instants, standard ROM techniques may not be a suitable choice, while displacement interpolation is expected to provide consistent and accurate predictions, generating synthetic but physically meaningful approximations at a negligible computational cost. For this problem, we consider a 3rd-order polynomial discretization on a series of increasingly finer meshes from 128^2 to 512^2 degrees of freedom. Time integration was performed using a classical 4th order Runge-Kutta scheme.

Moreover, to test the generalizability of the proposed procedure to the parameterized setting, we consider the parametric extension of the test case by changing the initial radius of the bubble in the following way:

$$R_k = 0.1 + k\Delta R \quad \text{with} \quad \Delta R = 0.005 \quad \text{and} \quad k = 0, \dots, 20. \quad (34)$$

An overview of the problem's dynamics corresponding to different values for the initial radius R and two different level of refinement (low-fidelity with 256^2 and high-fidelity with 512^2) is shown in Figure 5. If not specified otherwise, we will always consider the case $R = 0.11$ to test our framework for the Rider-Kothe vortex.

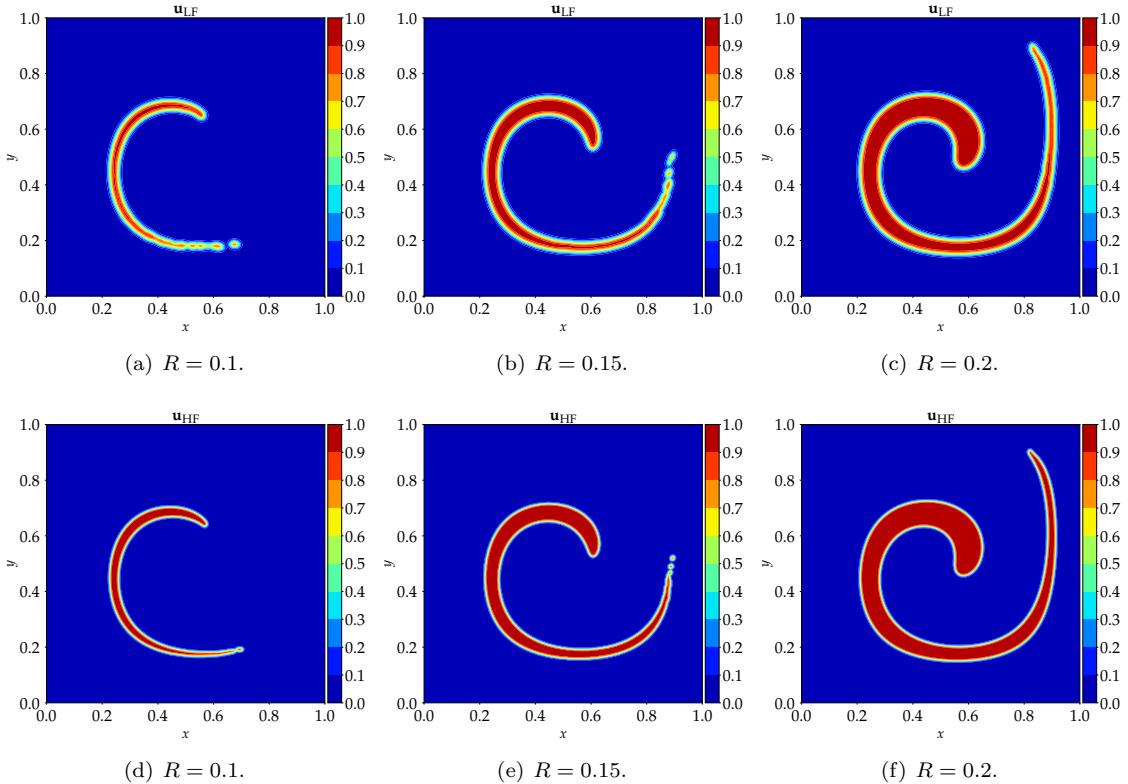


FIGURE 5. Low-fidelity (top) and high-fidelity (bottom) phase-field isocontours for different initial conditions of the Rider-Kothe vortex at $t = T/2$.

6.1.1. *Proper Orthogonal Decomposition and Displacement Interpolation.* Before presenting the performance of the novel strategies proposed in this work, we want to further motivate and numerically show the main reasons to exploit displacement interpolation instead of a classical POD-based reduced-order models. Here, we aim to highlight the limitations of standard linear reduction strategies in reconstructing the temporal evolution of the phase field in two-phase flows. Towards this goal, we consider the aforementioned Rider-Kothe vortex problem and compare the results obtained with POD projection of the high-fidelity solutions and via displacement interpolation.

We remark that we have introduced the nomenclature *checkpoints* for the set of snapshots used to perform the pairwise displacement interpolation. Thus, to provide a fair comparison with POD, the number of checkpoints used in the displacement interpolation will always match the number of snapshots available for the POD projection. Indeed, the checkpoints are the only *data* nominally available by the OT procedure as well as by the POD.

Figure 6 shows an example of the predicted phase field obtained exploiting the two strategies (POD and DI) with $N_c = 30$ checkpoints. It is evident that performing displacement interpolation between high-fidelity data produces more accurate results than using the POD basis. This expected improvement is indeed related to the spatial differences in the support regions between snapshots: the POD projection essentially computes a linear combination of the available modes leading to a noticeable smearing of the interface and intermediate unphysical values for the reconstructed field. In contrast, displacement interpolation correctly predicts values of either zero or one in the whole spatial domain, detecting with high accuracy the evolution of the moving feature and its sharp variation. In Figures 7 and 8, instead, we present a more quantitative evaluation of the relative

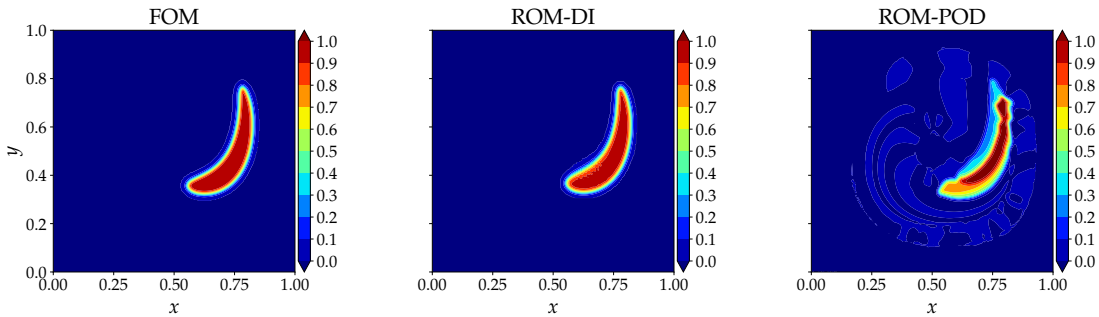


FIGURE 6. Phase field at $t \approx 0.2$ for the Rider-Kothe vortex (256×256). Left, FOM; center, DI ($N_c = 30$); right, POD projection ($N_c = 30$).

errors of displacement interpolation and POD projection varying the total number of checkpoints. We notice that, for a small number of checkpoints, the relative errors show only minor differences between the two approaches. However, as the number of checkpoints increases, displacement interpolation between consecutive data points provides significantly more accurate results compared to POD projection. In particular, note the clearly intermittent behavior at initial and late stages of the dynamics. In these regions, where the droplet moves at its highest speed, the POD projection struggles to accurately capture the dynamics of the problem, and provides seemingly better results only in reconstructing the states that have been used to construct the POD basis. Although displacement interpolation yields only modest improvements compared to POD projection in terms of relative error (see Figure 8), we emphasize that this observation is largely influenced by the specific error metric adopted. Such a metric may be partially misleading, as it does not fully capture the key features of interest in the solution, namely the interface morphology and the accuracy of the reconstructed phase-field values. For these reasons, in Figure 9, we analyze the problem from a more modeling-oriented perspective by examining the total area where $0.1 < \phi_1 < 0.9$, that in the case of bounded values, provides an approximation of the droplet's surface.

Specifically, Figure 9 shows that the general trend of the FOM behaves as expected for this problem: the droplet is initially circular, then stretches into a thin ligament, maximizing the total

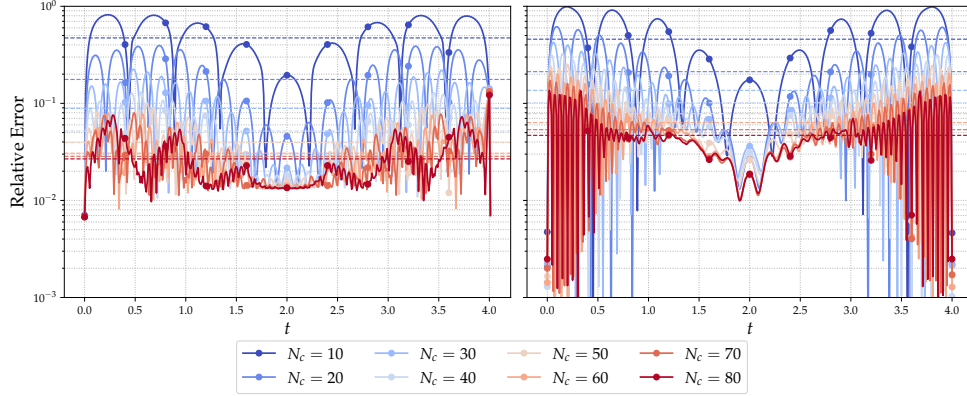


FIGURE 7. Relative error for DI (left) and POD projection (right) for the Rider-Kother vortex (256×256).

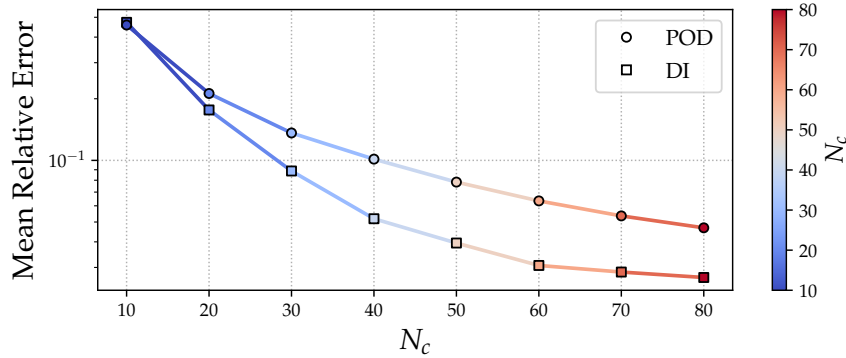


FIGURE 8. Mean relative error for DI and POD projection for the Rider-Kother vortex (256×256).

surface area, and finally returns toward its initial shape. The displacement interpolation approach captures this behavior accurately, while, in contrast, POD projection deviates significantly from the expected trend, particularly at the initial and final stages of the dynamics, where the prescribed advection velocity reaches its maximum. Furthermore, even in regions where common support exists, the POD projection essentially acts as a high-order interpolation, and even increasing the number of basis spanning the POD space, the benefits in accuracy are counteracted by the introduction of spurious oscillations near sharp features. This behavior is clearly visible in Figure 10, where we show a one-to-one comparison of the upper bounds of the phase field predicted by displacement interpolation and POD projection. It is evident that DI consistently remains very close to the FOM simulations, whereas the POD projection exhibits strong oscillations linked to unphysical behavior around the correct values.

6.1.2. MF-OT-ROM. In the previous section, we highlighted how POD-based ROMs perform poorly for advection-dominated problems, such as those arising in numerical simulations of two-phase flows. While POD can achieve reasonable results in terms of relative error, more case-specific metrics, such as boundedness and interfacial area, reveal significant deviations from the correct dynamics.

In this section, we consider the proposed extensions of the OT-based surrogate modeling for the simulation of two-phase flows. We begin with the MF-OT-ROM approach introduced previously, where displacement interpolation is used to interpolate the residuals between high- and low-fidelity

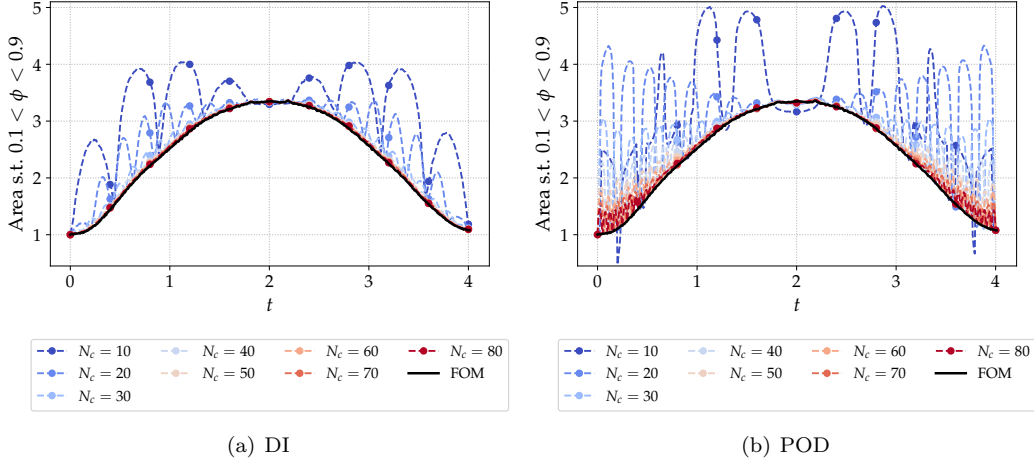


FIGURE 9. Normalised area of the spatial domain such that $0.1 < \phi_1 < 0.9$ using DI (left) and POD projection (right).

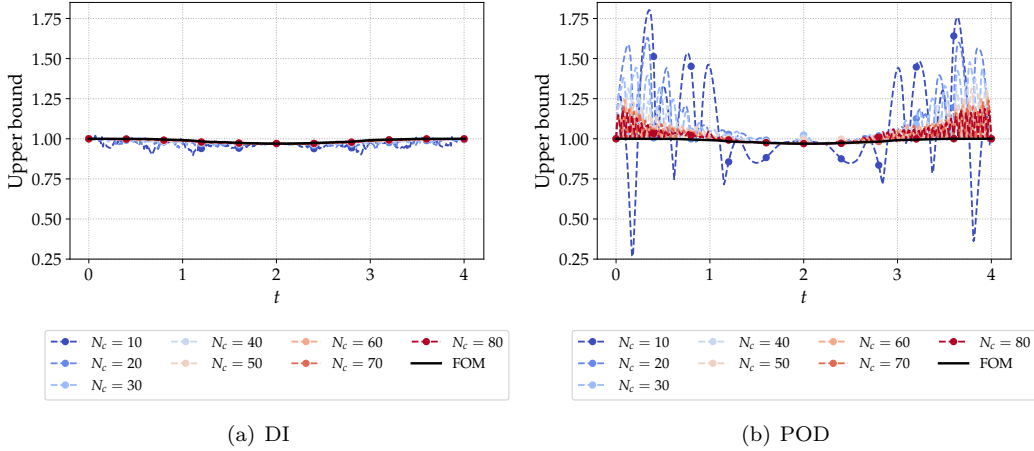


FIGURE 10. Maximum value of the predicted phase field as a function of time using DI (left) and POD projection (right).

solutions. The interpolated residual is then employed to *correct* the low-fidelity simulations in order to recover, as accurately as possible, an approximation of the high-fidelity solutions.

For this test case, we consider three levels of fidelity: 128×128 , 256×256 , and 512×512 , computing the pairwise residuals between the different grid resolutions.

As in the previous section, to perform a complete study on the performance of the strategy with respect to the available data, we vary the number of checkpoints used for the displacement interpolation. Figures 11 and 12 quantify the relative errors produced by the proposed approach, measured as the difference between the low-fidelity simulation (corrected or not via OT) and the high-fidelity simulation. In Figure 11, we show the relative error between low- and high-fidelity solutions as a function of time, varying the number of checkpoints. The uncorrected low-fidelity solution is shown in black, while a color gradient from blue to red indicates an increasing number of checkpoints. With relatively few checkpoints (e.g., $N_c = 10$), the corrected low-fidelity solution can locally increase the error relative to the high-fidelity solution, although the mean error decreases (see Figure 12). As the number of checkpoints increases, the relative error decreases throughout

the whole trajectory, demonstrating progressively better agreement with the high-fidelity solution. In Figure 12, we consider both settings with 128×128 and 256×256 exploited as low-fidelity,

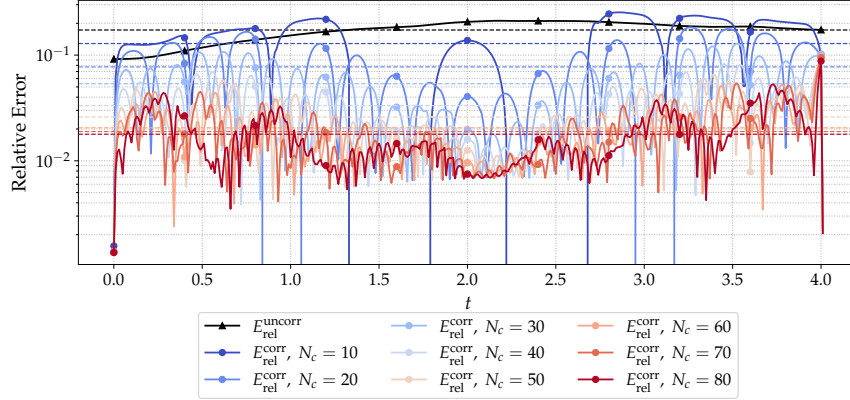


FIGURE 11. Relative error between low- and high-fidelity solutions w.r.t. different number of checkpoints for Rider-Kothe vortex with $R = 0.11$. Horizontal dashed lines represent the mean error for each temporal trajectory. Low-fidelity, 256×256 ; high-fidelity 512×512 .

and we investigate the decay of the mean error. Notice that the trend is almost identical between the two cases, but always over-performing the uncorrected approximations, suggesting that the correction is effective for both resolutions and that in both cases we are accurately capturing all the features from the dynamics. Indeed, by reporting the relative errors, the improvement obtained by correcting the 128×128 solution to match the 256×256 solution is, in relative terms, almost the same as that obtained by correcting the 256×256 solution to match the 512×512 solution. From

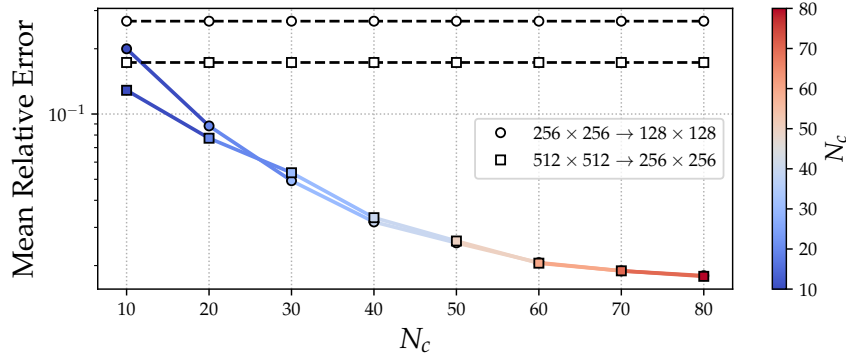


FIGURE 12. Mean relative errors against number of checkpoints.

a qualitative perspective, Figures 13 and 14 show the isolines $\phi_1 = 0.5$, representing the interface location, predicted by the corrected low-fidelity solutions, along with the low-fidelity (dashed black) and high-fidelity (dash-dotted black) references. In Figure 13, the 128×128 solution is considered as low-fidelity, whereas in Figure 14, the 256×256 solution serves as the low-fidelity reference, and increasing the number of checkpoints significantly improves in both cases the predicted interface location.

In Figure 15, we show the full predicted field for ϕ_1 near the top of the droplet at $t = 1.95$. The first row displays the high-fidelity simulation, while the second row shows the low-fidelity resolution,

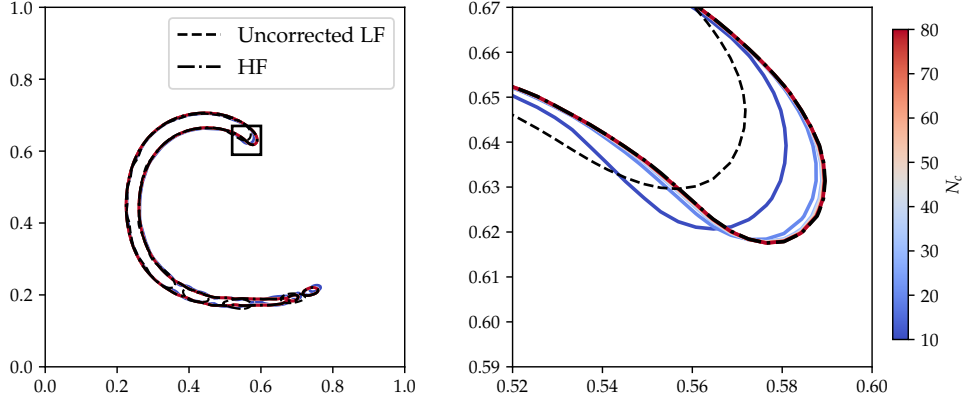


FIGURE 13. Isocontour of $\phi = 0.5$ for 256×256 HF (dash-dotted black), 128×128 LF (dashed black) and corrected LFs (color gradient) at $t = 1.95$.

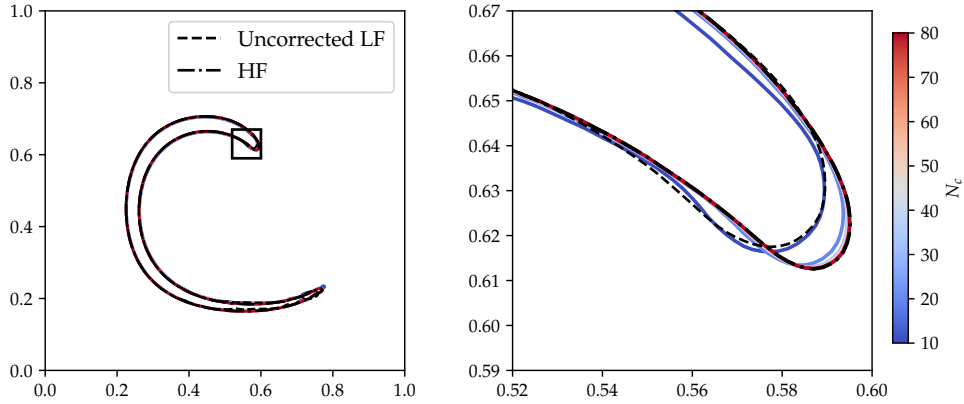


FIGURE 14. Isocontour of $\phi = 0.5$ for 512×512 HF (dash-dotted black), 256×256 LF (dashed black) and corrected LFs (color gradient) at $t = 1.95$.

where, from left to right, the amount of OT correction is increased: the left panel shows the uncorrected low-fidelity solution, while the center and right panels show the corrected low-fidelity solutions using $N_c = 10$ and $N_c = 80$ checkpoints, respectively. The nice performance of the methodology is already evident exploiting only 10 checkpoints, with the solution showing a significant improvement in terms of interface thickness. Finally, using $N_c = 80$ produces a corrected solution that is nearly indistinguishable from the high-fidelity simulation.

6.1.3. PMF-OT-ROM. In this section, we increase the complexity of the discussed benchmark by considering a fully parametric setting. In this scenario, two different strategies can be used to correct a low-fidelity simulation for a given parameter when no high-fidelity solution is readily available. The first approach consists of computing the residual from neighboring trajectories, interpolating this residual in parameter space, and then performing a second interpolation in time, reverting to the MF-OT-ROM approach presented earlier. The second strategy, instead, involves applying displacement interpolation directly to high-fidelity data from neighboring trajectories to generate a new high-fidelity trajectory for unseen parameters, which can then be used to correct the corresponding low-fidelity solution. We will focus on this latter approach for the remainder of the work as it has shown better stability properties in the resolution of the OT problem.

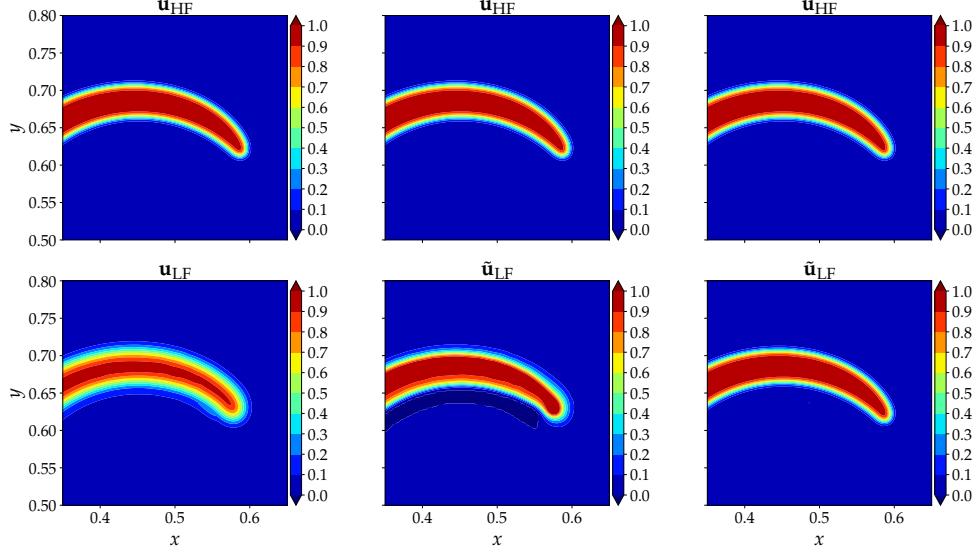


FIGURE 15. Comparison between 512×512 HF simulations (repeated on the top row) and different levels of 256×256 LF in the bottom row at $t = 1.95$. Specifically, from left to right: Uncorrected LF, Corrected LF with $N_c = 10$ and Corrected LF with $N_c = 80$.

In Figure 16 we report the relative error between the corrected low-fidelity solution and the validation high-fidelity solution for an unseen parametric trajectory. We can observe that increasing the number of checkpoints significantly decreases the errors throughout the whole dynamics. In Figure 17 we show the mean error over the entire trajectory, which further highlights the decrease in error as the number of checkpoints increases. Finally, in Figure 18, as a metrics which is

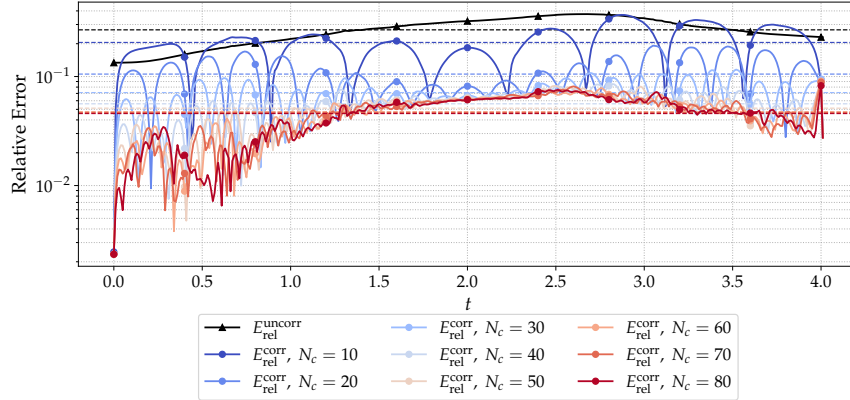


FIGURE 16. Relative error between low- and high-fidelity for different number of checkpoints for the Rider-Kothe vortex with unseen parameter $R = 0.11$. Horizontal dashed lines represent the mean error for each temporal trajectory. Low-fidelity, 128×128 ; high-fidelity 256×256 .

more specific for this problem, we investigate the upper bound and total interface's surface by comparing high-fidelity, uncorrected low-fidelity and a series of corrected low fidelities with the proposed approach with different number of checkpoints. Notice that as the number of checkpoints increase we obtain an almost perfect match in both quantities.

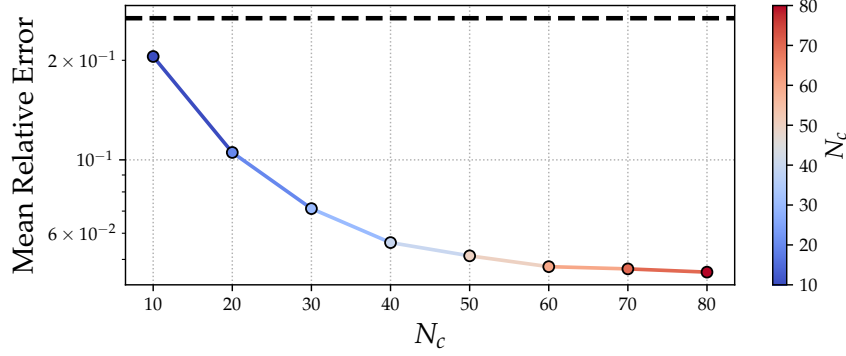


FIGURE 17. Mean relative errors against number of checkpoints for the unseen parameter $R = 0.11$. Low-fidelity, 128×128 ; high-fidelity 256×256 .

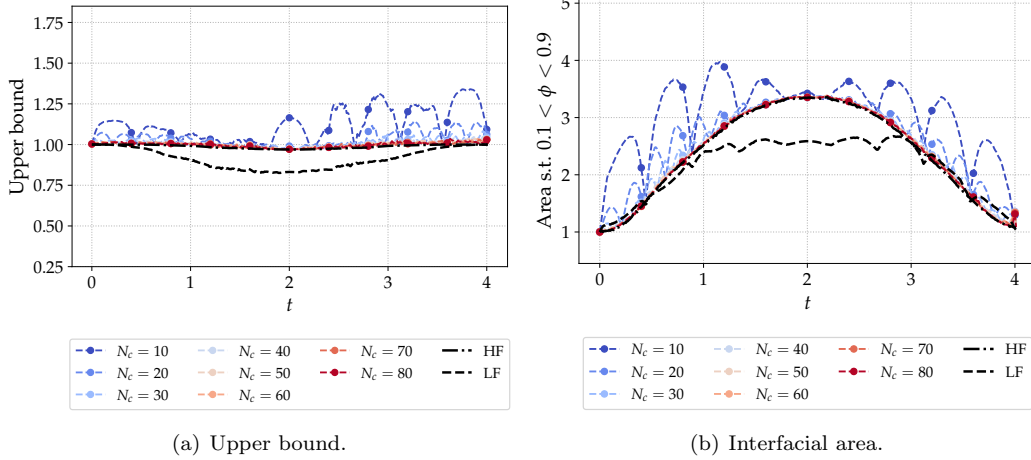


FIGURE 18. Maximum value of the predicted phase field as a function of time (left) and interfacial area (right). Dash-dotted line, HF; dashed, uncorrected LF; color gradient, corrected LFs. Low-fidelity, 128×128 ; high-fidelity 256×256 .

6.2. Rayleigh-Taylor instability. As an additional test case, we consider the simulation of a Rayleigh-Taylor instability, which occurs when an interface between two fluids with different densities experiences a pressure gradient opposing the density gradient. The computational domain is $[d \times 4d]$ with $d = 1$, and the interface is initially defined as the curve $y(x) = 2d + 0.1d \cos(2\pi x/d)$. The Rayleigh-Taylor instability is characterized by the Reynolds number $\text{Re} = (\rho_1 d^{3/2} \|\mathbf{g}\|^{1/2})/\mu$ and the Atwood number $\text{At} = (\rho_1 - \rho_2)/(\rho_1 + \rho_2)$ which are classically set to 3000 and 0.5, time is adimensionalized as $t^* = t/\sqrt{d/(\|\mathbf{g}\|\text{At})}$, while for the EOS relation in Equation (27) we chose the following parameters $\gamma_1 = \gamma_2 = 1.4$, $P_1^\infty = P_2^\infty = 6000$.

The Reynolds number characterizes the relative importance of inertial to viscous effects in the coupled system and is governed by gravity and the mixture viscosity, which is assumed constant across the two phases for this case. The Atwood number, on the other hand, quantifies the density contrast between the phases. When $\text{At} = 0$, the two phases have identical densities, whereas increasing values of the Atwood number correspond to progressively larger density ratios. As the Atwood number increases, one therefore expects the flow to develop increasingly complex interfacial patterns.

Concerning its parametric extension, we considered varying configurations corresponding to Atwood numbers in the following range:

$$\text{At}_k = 0.25 + k\Delta\text{At} \quad \text{with} \quad \Delta\text{At} = 0.025 \quad \text{and} \quad k = 0, \dots, 20. \quad (35)$$

An overview of the parametric problem's dynamics is shown in Figure 19. The top boundary is

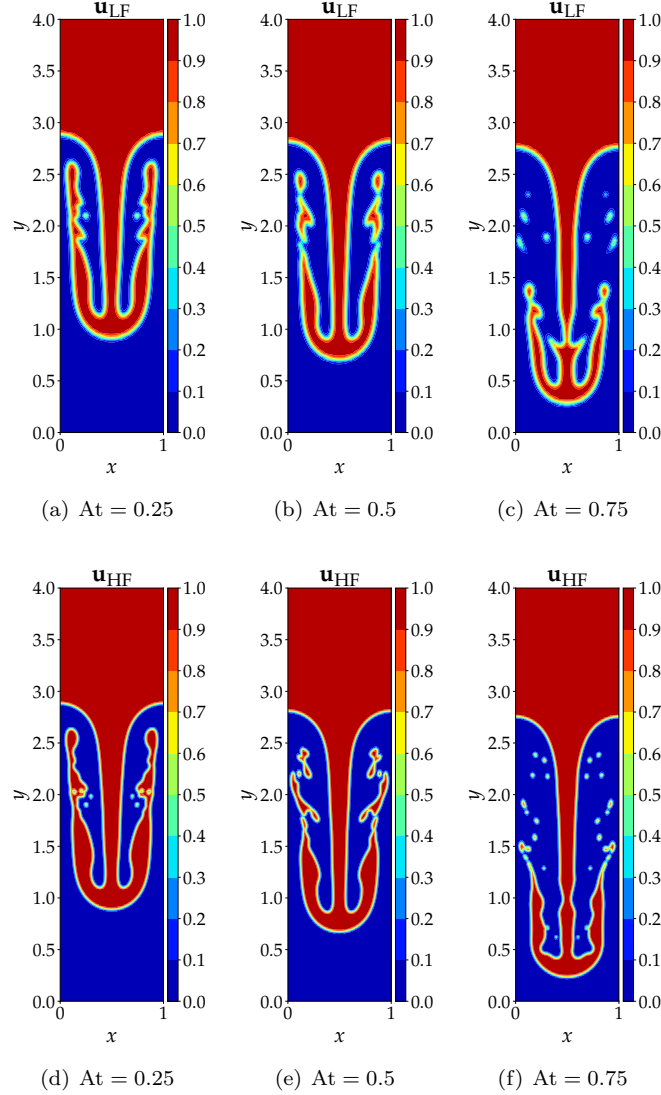


FIGURE 19. Phase-field isocontours at different Atwood numbers for the Rayleigh-Taylor instability at $t^* = 3.0$. First row: low-fidelity simulations. Second row: high-fidelity simulations.

treated as a Riemann-invariant boundary condition with zero velocity and constant pressure, the bottom boundary is a no-slip wall whereas slip-wall boundary conditions are prescribed on the other lateral sides of the domain. For this study, two different meshes with quadrilateral elements were considered, involving 40k and 160k degrees of freedom. A 4th order Runge-Kutta scheme was used for time integration. If not specified otherwise, we will always consider the $\text{At} = 0.35$ case to test our framework for the Rayleigh-Taylor Instability.

6.2.1. *MF-OT-ROM*. Similarly to the previous test case, we aim to quantify the relative errors between the low- and high-fidelity solutions, both with and without DI correction. In Figure 20, we report the relative error as a function of time for different numbers of checkpoints.

A markedly different trend emerges compared to the previous test case: here, the dynamics *accelerates* over time. Initially, the interface evolves relatively slowly, but it subsequently accelerates due to gravitational effects, leading to complex breakup patterns. This behavior is also reflected in the MF-OT-ROM procedure, as the errors tend to grow as time progresses. This expresses that a more involved regression of the virtual time α may be needed to better capture the accelerating dynamics, but the current approximation already provides a significant improvement over the uncorrected low-fidelity solution, even with a limited amount of data, and increasing the number of checkpoints significantly improves the overall accuracy of the method, consistently with the behavior observed in the previous test case.

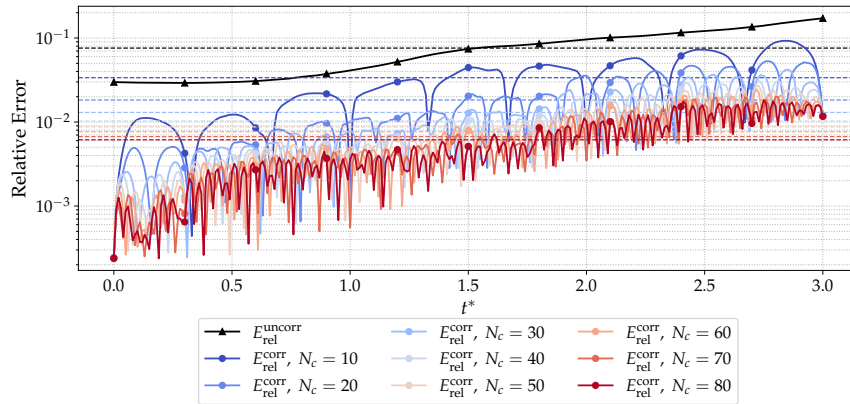


FIGURE 20. Relative error between low- and high-fidelity for different number of checkpoints for Rayleigh-Taylor instability with $At = 0.35$. Horizontal dashed lines represent the mean error for each temporal trajectory.

In Figure 21, we present the full predicted field of ϕ_1 for the Rayleigh-Taylor instability problem. Each panel is split into two halves, where the high-fidelity solution is mirrored against the corresponding low-fidelity prediction (either corrected or uncorrected) to facilitate visual comparison. From left to right, the level of OT correction increases. The left panel displays the uncorrected low-fidelity solution, while the central and right panels show the corrected low-fidelity solutions obtained with $N_c = 10$ and $N_c = 80$ checkpoints, respectively.

We observe that even for the smallest value of N_c considered here, the OT-based correction substantially improves the overall prediction. Increasing the number of checkpoints to $N_c = 80$ further enhances the accuracy, to the point that the corrected low-fidelity solution becomes almost indistinguishable from the high-fidelity one.

More importantly, for this specific problem, where breakup phenomena are widespread, we assess the capability of the MF-OT-ROM approach to accurately predict the total interfacial surface from a quantitative perspective. In Figure 22, we report the normalized interface surface as a function of time for both fidelities, considering the uncorrected and OT-corrected low-fidelity solutions. First, the temporal evolution clearly reflects the breakup dynamics. At early times, the interface between the two phases is relatively smooth and the total surface is limited. As the instability develops, gravitational effects enhance mixing, generating complex structures and significantly increasing the contact area between the phases. Second, a classical resolution effect can be observed: coarse simulations are generally unable to capture small-scale features, such as vortices and thin interfacial ligaments. As a consequence, the low-fidelity solution systematically under-predicts the total interfacial area.

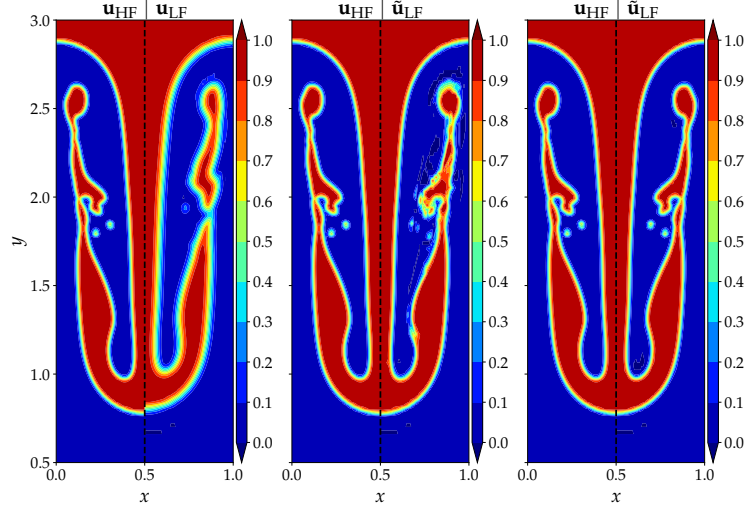


FIGURE 21. Phase field isocontours for Rayleigh-Taylor instability at $t^* = 2.95$ and $At = 0.35$. In each subfigure the left field is given by the HF solution. In each subfigure, on the right, are shown respectively: LF solution, corrected LF solution with $N_c = 10$ and corrected LF solution with $N_c = 80$.

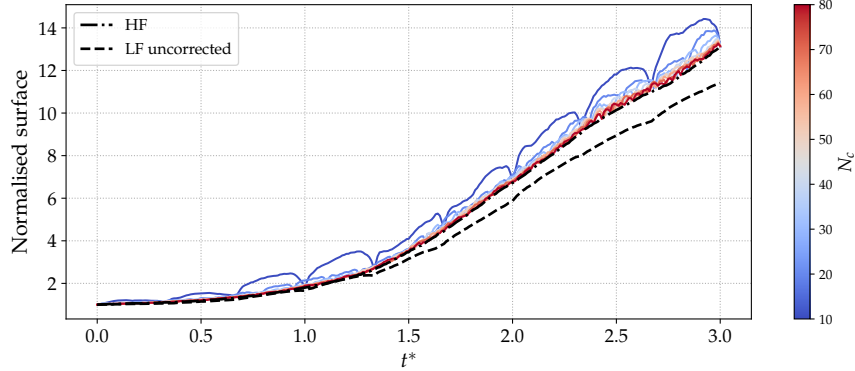


FIGURE 22. Normalized interfacial surface as a function of time for the Rayleigh-Taylor instability problem. High-fidelity solution is represented by the dash-dotted black line, uncorrected LF by the dashed black line and corrected LFs are shown using color gradient from blue to red for increasing values of N_c .

Finally, as the number of checkpoints N_c increases, the MF-OT-ROM prediction progressively converges toward the reference high-fidelity solution, confirming the effectiveness of the OT-based correction in recovering fine-scale interfacial dynamics. Interestingly, the MF-OT-ROM curve approaches the HF reference from above. This behavior may be attributed to the regularization employed within the OT solver. Indeed, as observed in the middle panel of Figure 21, a limited number of checkpoints produces a solution that appears less smooth. This residual lack of regularity can artificially increase the small-scale oscillations at the interface, ultimately leading to a slight over-prediction of the total interfacial area.

6.2.2. *PMF-OT-ROM*. In this last part we test the parametric multi-fidelity approach for the Rayleigh-Taylor Instability problem. It is worth noting that we expect significant variations in the dynamics for different parameters.

In Figure 23 we compare how the relative error behaves for different number of checkpoints. Normally, we would expect that for larger numbers of checkpoints the error would decrease. This is generally the case but in a different manner depending on the problem’s dynamics. In fact, at early stages, the improvement given by considering more checkpoints is significant. The initial dynamics, in fact, is very similar across the different parameters as the initial condition for the phase field is exactly the same across the whole dataset. However, as the dynamics of the problem unfolds, the type of breakups obtained at later stages is significantly different. At those stages, considering more checkpoints does not significantly improve the prediction of the OT solver. This clearly indicates that, as already observed previously, the benefit of using more checkpoints to reconstruct the fast-dynamical features of the problem is limited by the naive choice of the linear interpolator for the virtual time α . The same concept in terms of mean error can be seen in Figure 24, where we can still observe that the error decrease by increasing the number of checkpoints used in the OT strategy, but at a slower rate. Within this framework we also modified the total number of snapshots at disposal

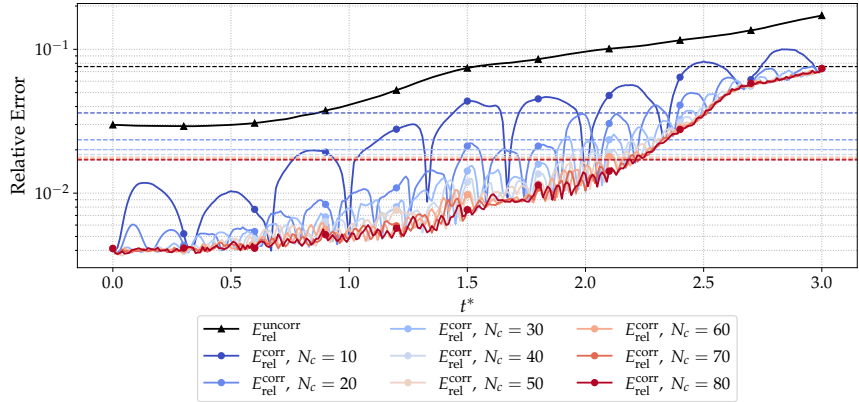


FIGURE 23. Relative error between low-fidelity and high-fidelity for different number of checkpoints. Horizontal dashed lines represent the mean error for each temporal trajectory.

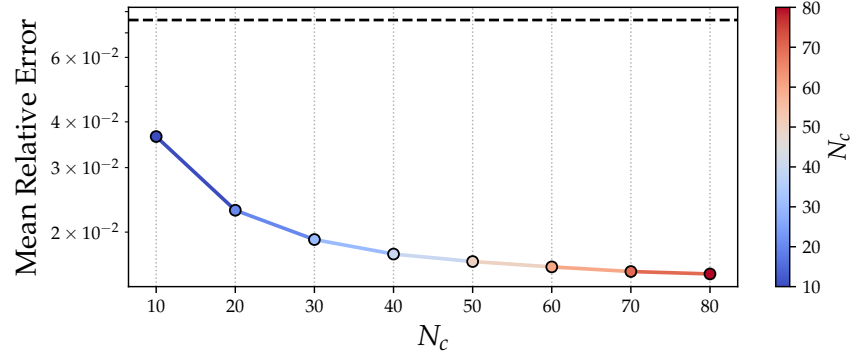


FIGURE 24. Mean relative errors against number of checkpoints.

so that we can observe the same trends in terms of parametric refinements. In Figure 25 we compare how the relative error behaves for different number of checkpoints and different size of the nominal dataset. Normally, we would expect that given more data the error would decrease. In this scenario, at late stages of the problem’s dynamics, considering more data improves the prediction of the OT solver, even better when a large number of checkpoints is considered (left panel of Figure 25). The

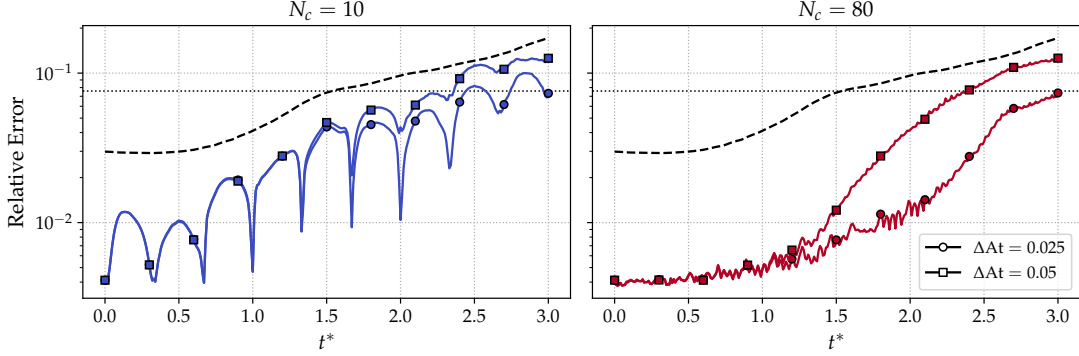


FIGURE 25. Relative error between low- and high-fidelity using the full dataset (circles) and half of it (squares). Dashed black line, uncorrected LF solution; dotted line, mean relative error for uncorrected LF solution. Left, $N_c = 10$; right, $N_c = 80$.

same concept in terms of mean error is shown in Figure 26 where we can observe that indeed the error decrease both by enlarging the initial dataset and by increasing the number of checkpoints used in the OT solver. In general it is then interesting to notice that a certain tradeoff between temporal and parametric refinements is necessary in order to achieve an optimal result. As a more informative

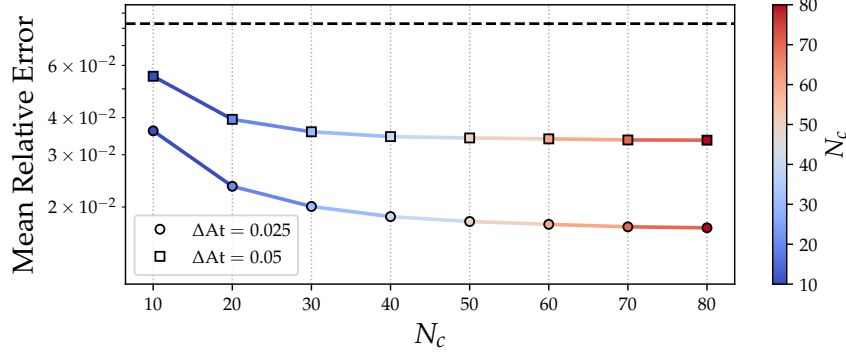


FIGURE 26. Mean relative errors against number of checkpoints using the full dataset (circles) and half of it (squares).

metric for this test case, we examine the total interface surface area integrated over the domain as a function of time. This quantity is reported in Figure 27, where we compare the predictions obtained with different numbers of checkpoints and different levels of parametric refinement.

In the early stages of the evolution, even a relatively small number of checkpoints ($N_c = 10$) is sufficient to accurately capture the interface dynamics. However, as time progresses and increasingly complex breakup events occur, discrepancies between the OT prediction and the HF solution become more pronounced. This deviation reflects the growing complexity of the interface topology, which is more challenging to reconstruct with a limited number of trajectories.

The agreement can be improved by increasing the number of trajectories in the parametric space, which enhances the resolution of the transported structures. Nevertheless, despite this refinement, we are not able to achieve the same level of agreement observed with the MF-OT-ROM approach applied exclusively in time (compare with Figure 22). In Figure 28 we compare the fields in the parametric setting as well. We can notice that for $N_c = 10$ the differences are quite noticeable but if we increase the number of checkpoints to $N_c = 80$ we obtain a quite good agreement between the high-fidelity solution and the OT-corrected low-fidelity one. Similarly to the predicted total

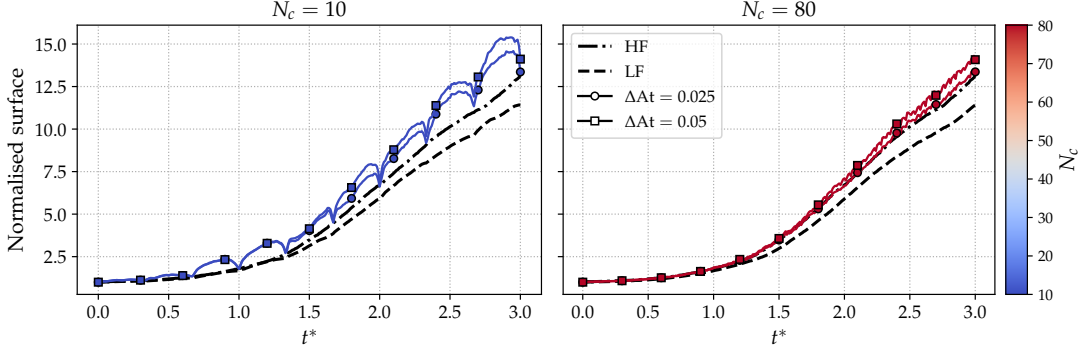


FIGURE 27. Normalized interface area predicted using the full dataset (circles) and half of it (squares). Left, $N_c = 10$; right, $N_c = 80$.

interfacial area, we are obtaining a good prediction in the parametric setting too although not as accurate as the single parametric multi-fidelity approach presented earlier. In the previous sections,

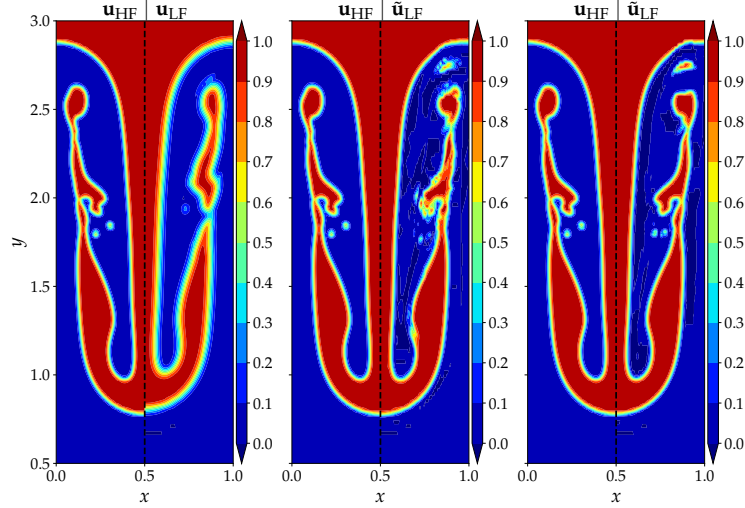


FIGURE 28. Phase field isocontours for Rayleigh-Taylor instability at $t^* = 2.95$ and $At = 0.35$. In each subfigure the left field is given by the HF solution. In each subfigure, on the right, are shown respectively: LF solution, corrected LF solution with $N_c = 10$ and corrected LF solution with $N_c = 80$.

we presented several combinations of OT-based approaches (MF-OT-ROM and PMF-OT-ROM) and different test cases (Rider-Kothe vortex and Rayleigh-Taylor instability). In all these analyses, however, we considered only a single test parameter to validate the proposed approaches. In this final section, we focus on investigating how the most general approach (PMF-OT-ROM) performs in the most challenging scenario (Rayleigh-Taylor instability) across different parametric settings. In particular, for this problem, we expect increasingly complex dynamics as the Atwood number is raised. Previous analyses were performed at $At = 0.35$. In the present study, we additionally consider $At = 0.5$ and $At = 0.65$.

Figure 29 presents a qualitative comparison of high-fidelity versus corrected low-fidelity solutions for the different Atwood numbers. For relatively small Atwood numbers (left panel), the breakups are mild, with the high-fidelity solution predicting very thin ligaments and a small number of dispersed droplets. As the Atwood number increases, more complex interfacial patterns emerge, making it

challenging for the reduced model to capture all fine-scale details accurately. Nevertheless, the large-scale dynamics, such as the position of the lower plume and the overall shape of the dominant interfacial structures, are correctly predicted. Figure 30 shows the relative error for two Atwood

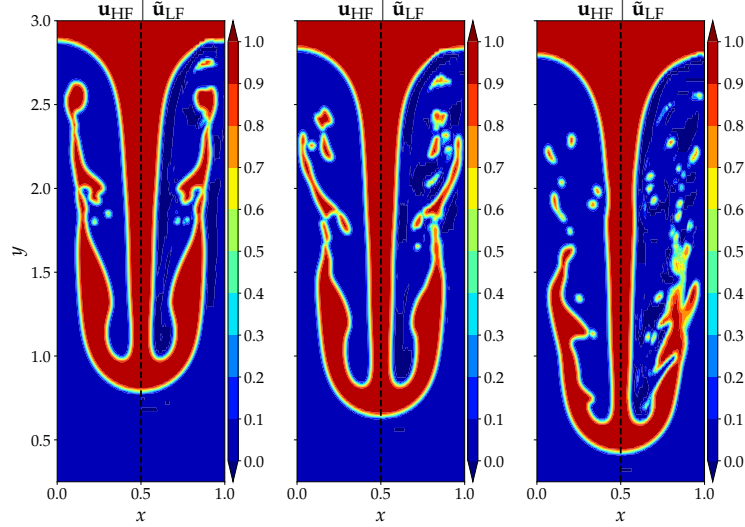


FIGURE 29. Phase-field isocontours for the Rayleigh-Taylor instability at $t^* = 2.95$ for different Atwood numbers. In each subfigure, the left field corresponds to the HF solution, and the right shows the corrected LF solution with $N_c = 80$. From left to right: $At = 0.35, 0.5, 0.65$.

numbers. Although a large number of checkpoints is used, increasing the parametric sampling does not significantly improve the predictions for high Atwood numbers in the late stages of the Rayleigh-Taylor instability. This behavior is expected due to the highly complex breakup dynamics that occur at larger Atwood numbers. In terms of predicted interfacial area, Figure 31 shows good agreement

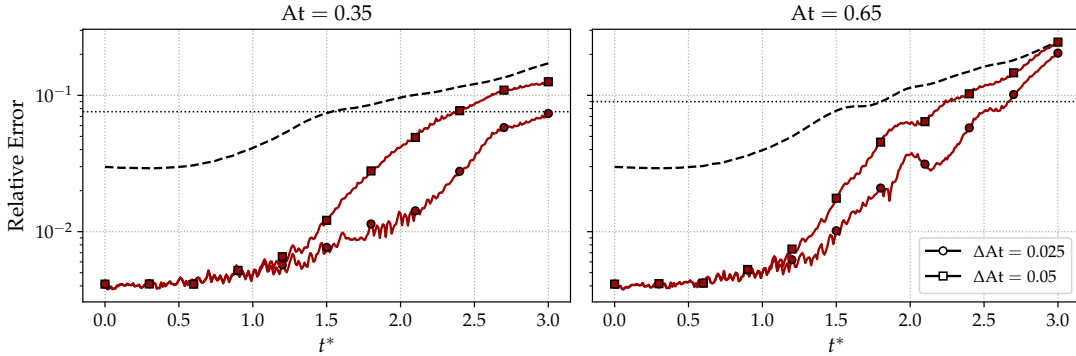


FIGURE 30. Relative error between low- and high-fidelity solutions using the full dataset (circles) and half of it (squares) with $N_c = 80$. Dashed black line: uncorrected LF solution; dotted black line: mean relative error of the uncorrected LF solution. Left, $At = 0.35$; right, $At = 0.65$.

between the best-performing model ($N_c = 80$ and $\Delta At = 0.025$) and the high-fidelity solution. For $At = 0.35$, the dynamics are accurately captured throughout the simulation. For $At = 0.65$, the interfacial area is well approximated up to $t^* = 2.5$, after which complex breakup events lead to a deterioration of the reduced solution.

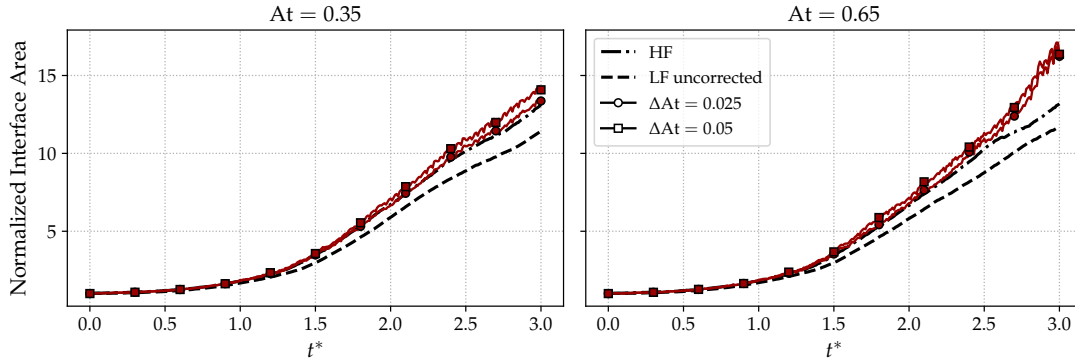


FIGURE 31. Normalized interfacial area predicted using the full dataset (circles) and half of it (squares) with $N_c = 80$. Left, $At = 0.35$; right, $At = 0.65$.

7. CONCLUSIONS AND PERSPECTIVES

In this paper, we have introduced two extensions to the Optimal Transport-based ROM framework. The multi-fidelity residual interpolation provides a method for correcting low-fidelity models by interpolating the HF-LF discrepancy field in time using displacement interpolation. The parametric displacement interpolation extends the framework to handle additional physical parameters beyond time, enabling prediction at unseen parameter values through a combination of parametric and temporal interpolation. For multi-fidelity parametric problems, we presented two strategies: interpolating the HF solution directly or interpolating the residual field in parameter space. This provides a computationally efficient and flexible approach for exploring parameter-dependent systems.

The mathematical formulation of these frameworks is general and can be applied to a wide range of problems governed by PDEs. By framing the discussion in the context of challenging diffuse-interface methods, we highlight the potential of these methods to handle complex, nonlinear dynamics involving moving fronts and interfaces.

Several directions for future work can be identified. First, the selection of training parameters and time checkpoints could be made adaptive, using error estimators to place computational effort where it is most needed. Second, the linear interpolation of the OT map in parameter space could be extended to barycentric interpolation for multiple parameters. Third, machine learning methods such as Gaussian Process Regression could be used to learn the mapping from physical parameters to the OT plans or interpolation weights. Finally, numerical validation on two-phase flow modelling problems, will quantify the performance and limitations of the proposed frameworks.

ACKNOWLEDGMENTS

This work was partially supported by the European Union - NextGenerationEU, in the framework of the iNEST - Interconnected Nord-Est Innovation Ecosystem (iNEST ECS00000043 - CUP G93C22000610007). The authors also acknowledge the support of the INdAM-GNCS.

REFERENCES

- [1] Martial Agueh and Guillaume Carlier. Barycenters in the Wasserstein space. *SIAM Journal on Mathematical Analysis*, 43(2):904–924, 2011. doi:[10.1137/100805741](https://doi.org/10.1137/100805741).
- [2] Jabir Al-Salami, Mohamed M Kamra, and Changhong Hu. A high order flux reconstruction interface capturing method with a phase field preconditioning procedure. *Journal of Computational Physics*, 438:110376, 2021.
- [3] Grégoire Allaire, Sébastien Clerc, and Samuel Kokh. A five-equation model for the simulation of interfaces between compressible fluids. *Journal of Computational Physics*, 181:577–616, 2002.

- [4] David Amsallem, Matthew J. Zahr, and Charbel Farhat. Nonlinear model order reduction based on local reduced-order bases. *International Journal for Numerical Methods in Engineering*, 92(10):891–916, 2012. doi:[10.1002/nme.4371](https://doi.org/10.1002/nme.4371).
- [5] Florian Arbes, Constantin Greif, and Karsten Urban. The Kolmogorov N-width for linear transport: Exact representation and the influence of the data. *Advances in Computational Mathematics*, 51(2):13, 2025. doi:[10.1007/s10444-025-10224-0](https://doi.org/10.1007/s10444-025-10224-0).
- [6] Ivo Babuska, Fabio Nobile, and Raúl Tempone. A stochastic collocation method for elliptic partial differential equations with random input data. *SIAM Journal on Numerical Analysis*, 45(3):1005–1034, 2007. doi:[10.1137/050645142](https://doi.org/10.1137/050645142).
- [7] Beatrice Battisti, Tobias Blickhan, Guillaume Enchery, Virginie Ehrlacher, Damiano Lombardi, and Olga Mula. Wasserstein model reduction approach for parametrized flow problems in porous media. *ESAIM: Proceedings and Surveys*, 73:28–47, 2023. doi:[10.1051/proc/202373028](https://doi.org/10.1051/proc/202373028).
- [8] Peter Benner, Serkan Gugercin, and Karen Willcox. A survey of projection-based model reduction methods for parametric dynamical systems. *SIAM Review*, 57(4):483–531, 2015. doi:[10.1137/130932715](https://doi.org/10.1137/130932715).
- [9] Tobias Blickhan. A registration method for reduced basis problems using linear optimal transport. *SIAM Journal on Scientific Computing*, 46(5):A3177–A3204, 2024. doi:[10.1137/23m1570715](https://doi.org/10.1137/23m1570715).
- [10] Nicolas Boullé, Patrick E. Farrell, and Alberto Paganini. Control of Bifurcation Structures using Shape Optimization. *SIAM Journal on Scientific Computing*, 44(1):A57–A76, 2022. doi:[10.1137/21M1418708](https://doi.org/10.1137/21M1418708).
- [11] Annalisa Buffa, Yvon Maday, Anthony T. Patera, Christophe Prud’homme, and Gabriel Turinici. A priori convergence of the Greedy algorithm for the parametrized reduced basis method. *ESAIM: Mathematical Modelling and Numerical Analysis*, 46(3):595–603, 2012. doi:[10.1051/m2an/2011056](https://doi.org/10.1051/m2an/2011056).
- [12] Anindya Chatterjee. An introduction to the proper orthogonal decomposition. *Current Science*, 78(7):808–817, 2000.
- [13] Peng Chen, Alfio Quarteroni, and Gianluigi Rozza. Reduced Basis Methods for Uncertainty Quantification. *SIAM/ASA Journal on Uncertainty Quantification*, 5(1):813–869, 2017. doi:[10.1137/151004550](https://doi.org/10.1137/151004550).
- [14] Pao-Hsiung Chiu and Yan-Ting Lin. A conservative phase field method for solving incompressible two-phase flows. *Journal of Computational Physics*, 230:185–204, 2011.
- [15] Albert Cohen and Ronald DeVore. Kolmogorov widths under holomorphic mappings. *IMA Journal of Numerical Analysis*, page dru066, 2015. doi:[10.1093/imanum/dru066](https://doi.org/10.1093/imanum/dru066).
- [16] Henry Collis, Deniz A Bezin, Shahab Mirjalili, and Ali Mani. A thermodynamically consistent and robust four-equation model for multi-phase multi-component compressible flows using enotype schemes including interface regularization. *arXiv preprint arXiv:2504.14063*, 2025.
- [17] Paolo Conti, Mengwu Guo, Andrea Manzoni, Attilio Frangi, Steven L. Brunton, and J. Nathan Kutz. Multi-fidelity reduced-order surrogate modelling. *Proceedings of the Royal Society A: Mathematical, Physical and Engineering Sciences*, 480(2283):20230655, 2024. doi:[10.1098/rspa.2023.0655](https://doi.org/10.1098/rspa.2023.0655).
- [18] Simona Cucchiara, Angelo Iollo, Tommaso Taddei, and Haysam Telib. Model order reduction by convex displacement interpolation. *Journal of Computational Physics*, 514:113230, 2024. doi:[10.1016/j.jcp.2024.113230](https://doi.org/10.1016/j.jcp.2024.113230).
- [19] Marco Cuturi. Sinkhorn distances: Lightspeed computation of optimal transport. In C.J. Burges, L. Bottou, M. Welling, Z. Ghahramani, and K.Q. Weinberger, editors, *Advances in Neural Information Processing Systems*, volume 26. Curran Associates, Inc., 2013.
- [20] Minh-Hieu Do, Jean Feydy, and Olga Mula. Sparse Wasserstein Barycenters and Application to Reduced Order Modeling. *Journal of Scientific Computing*, 102(3):64, 2025. doi:[10.1007/s10915-024-02766-0](https://doi.org/10.1007/s10915-024-02766-0).

- [21] Virginie Ehrlicher, Damiano Lombardi, Olga Mula, and François-Xavier Vialard. Nonlinear model reduction on metric spaces. Application to one-dimensional conservative PDEs in Wasserstein spaces. *ESAIM: Mathematical Modelling and Numerical Analysis*, 54(6):2159–2197, 2020. doi:[10.1051/m2an/2020013](https://doi.org/10.1051/m2an/2020013).
- [22] Stefania Fresca, Andrea Manzoni, and Luca Dedè. A comprehensive deep learning-based approach to reduced order modeling of nonlinear time-dependent parametrized PDEs. *Journal of Scientific Computing*, 87(2):1–42, 2021.
- [23] Rudy Geelen and Karen Willcox. Localized non-intrusive reduced-order modelling in the operator inference framework. *Philosophical Transactions of the Royal Society A: Mathematical, Physical and Engineering Sciences*, 380(2229):20210206, 2022. doi:[10.1098/rsta.2021.0206](https://doi.org/10.1098/rsta.2021.0206).
- [24] Matteo Giacomini and Antonio Huerta. A surrogate model for topology optimisation of elastic structures via parametric autoencoders. *Computer Methods in Applied Mechanics and Engineering*, 448:118503, 2026. doi:[10.1016/j.cma.2025.118503](https://doi.org/10.1016/j.cma.2025.118503).
- [25] Silke Glas, Anthony T. Patera, and Karsten Urban. A reduced basis method for the wave equation. *International Journal of Computational Fluid Dynamics*, 34(2):139–146, 2020. doi:[10.1080/10618562.2019.1686486](https://doi.org/10.1080/10618562.2019.1686486).
- [26] Francis H Harlow and Anthony A Amsden. Fluid dynamics. A LASL monograph. Technical report, Los Alamos National Lab (LANL), Los Alamos, NM (United States), 1971.
- [27] Martin Hess, Alessandro Alla, Annalisa Quaini, Gianluigi Rozza, and Max Gunzburger. A localized reduced-order modeling approach for PDEs with bifurcating solutions. *Computer Methods in Applied Mechanics and Engineering*, 351:379–403, 2019. doi:[10.1016/j.cma.2019.03.050](https://doi.org/10.1016/j.cma.2019.03.050).
- [28] Jan S. Hesthaven, Gianluigi Rozza, and Benjamin Stamm. *Certified Reduced Basis Methods for Parametrized Partial Differential Equations*. SpringerBriefs in Mathematics. Springer International Publishing, 2016. doi:[10.1007/978-3-319-22470-1](https://doi.org/10.1007/978-3-319-22470-1).
- [29] Jan S. Hesthaven, Benjamin Peherstorfer, and Benjamin Unger. Nonlinear model reduction for transport-dominated problems. 2026. doi:[10.48550/arXiv.2602.01397](https://doi.org/10.48550/arXiv.2602.01397).
- [30] Amanda A. Howard, Mauro Perego, George Em Karniadakis, and Panos Stinis. Multifidelity deep operator networks for data-driven and physics-informed problems. *Journal of Computational Physics*, 493:112462, 2023. doi:[10.1016/j.jcp.2023.112462](https://doi.org/10.1016/j.jcp.2023.112462).
- [31] Ziyang Huang and Eric Johnsen. A consistent and conservative phase-field method for compressible multiphase flows with shocks. *Journal of Computational Physics*, 488:112195, 2023.
- [32] Mohammed Ibrahim, Methma Rajamuni, Chuangde Zhang, Li Chen, John Young, and Fang-Bao Tian. A conservative phase-field lattice boltzmann method for boiling heat transfer at high density ratios. *Physics of Fluids*, 37(5), 2025.
- [33] Angelo Iollo and Tommaso Taddei. Mapping of coherent structures in parameterized flows by learning optimal transportation with Gaussian models. *Journal of Computational Physics*, 471:111671, 2022. doi:[10.1016/j.jcp.2022.111671](https://doi.org/10.1016/j.jcp.2022.111671).
- [34] V. Isakov. *Inverse Problems for Partial Differential Equations*. Applied Mathematical Sciences. Springer International Publishing, 2017.
- [35] Suhas S Jain. Accurate conservative phase-field method for simulation of two-phase flows. *Journal of Computational Physics*, 469:111529, 2022.
- [36] Tianyu Jin, Zhichao Peng, and Yang Xiang. Adaptive and hybrid reduced order models to mitigate Kolmogorov barrier in a multiscale kinetic transport equation, 2025.
- [37] L. V. Kantorovich. On the translocation of masses. *Journal of Mathematical Sciences*, 133(4):1381–1382, 2006. ISSN 1573-8795. doi:[10.1007/s10958-006-0049-2](https://doi.org/10.1007/s10958-006-0049-2). URL <http://dx.doi.org/10.1007/s10958-006-0049-2>.
- [38] Moaad Khamlich, Federico Pichi, Michele Girfoglio, Annalisa Quaini, and Gianluigi Rozza. Optimal transport-based displacement interpolation with data augmentation for reduced order modeling of nonlinear dynamical systems. *Journal of Computational Physics*, 531:113938, 2025. doi:[10.1016/j.jcp.2025.113938](https://doi.org/10.1016/j.jcp.2025.113938).
- [39] Toni Lassila, Andrea Manzoni, Alfio Quarteroni, and Gianluigi Rozza. Generalized reduced basis methods and n-width estimates for the approximation of the solution manifold of parametric

- pdes. *Bollettino dell'Unione Matematica Italiana*, 6(1):113–135, 2 2013. URL <http://eudml.org/doc/294013>.
- [40] Kookjin Lee and Kevin T. Carlberg. Model reduction of dynamical systems on nonlinear manifolds using deep convolutional autoencoders. *Journal of Computational Physics*, 404:108973, 2020. doi:[10.1016/j.jcp.2019.108973](https://doi.org/10.1016/j.jcp.2019.108973).
- [41] Andrea Manzoni, Alfio Quarteroni, and Sandro Salsa. *Optimal Control of Partial Differential Equations: Analysis, Approximation, and Applications*, volume 207 of *Applied Mathematical Sciences*. Springer International Publishing, Cham, 2021. doi:[10.1007/978-3-030-77226-0](https://doi.org/10.1007/978-3-030-77226-0).
- [42] Robert J. McCann. A convexity principle for interacting gases. *Advances in Mathematics*, 128(1):153–179, 1997. doi:[10.1006/aima.1997.1634](https://doi.org/10.1006/aima.1997.1634).
- [43] Shahab Mirjalili, Christopher B Ivey, and Ali Mani. A conservative diffuse interface method for two-phase flows with provable boundedness properties. *Journal of Computational Physics*, 401:109006, 2020.
- [44] Shahab Mirjalili, Suhas S Jain, and Ali Mani. A computational model for interfacial heat and mass transfer in two-phase flows using a phase field method. *International Journal of Heat and Mass Transfer*, 197:123326, 2022.
- [45] Gaspard Monge. Mémoire sur la théorie des déblais et des remblais. *Histoire de l'Académie Royale des Sciences*, 1781.
- [46] Olga Mula. Inverse Problems: A Deterministic Approach Using Physics-Based Reduced Models. In Michael Hinze, J. Nathan Kutz, Olga Mula, Karsten Urban, Maurizio Falcone, and Gianluigi Rozza, editors, *Model Order Reduction and Applications: Cetraro, Italy 2021*, pages 73–124. Springer Nature Switzerland, Cham, 2023. doi:[10.1007/978-3-031-29563-8_2](https://doi.org/10.1007/978-3-031-29563-8_2).
- [47] Monica Nonino and Davide Torlo. Calibration-Based ALE Model Order Reduction for Hyperbolic Problems with Self-Similar Travelling Discontinuities. *Journal of Scientific Computing*, 101(3):60, 2024. doi:[10.1007/s10915-024-02694-z](https://doi.org/10.1007/s10915-024-02694-z).
- [48] Mario Ohlberger and Stephan Rave. Reduced Basis Methods: Success, Limitations and Future Challenges. 2016. doi:[10.48550/arXiv.1511.02021](https://doi.org/10.48550/arXiv.1511.02021).
- [49] Benjamin Peherstorfer. Model reduction for transport-dominated problems via online adaptive bases and adaptive sampling. *SIAM Journal on Scientific Computing*, 42(5):A2803–A2836, 2020. doi:[10.1137/19M1257275](https://doi.org/10.1137/19M1257275).
- [50] Benjamin Peherstorfer. Breaking the Kolmogorov Barrier with Nonlinear Model Reduction. *Notices of the American Mathematical Society*, 69(05), 2022. doi:[10.1090/noti2475](https://doi.org/10.1090/noti2475).
- [51] Benjamin Peherstorfer, Karen Willcox, and Max Gunzburger. Survey of multifidelity methods in uncertainty propagation, inference, and optimization. *SIAM Review*, 60(3):550–591, 2018. doi:[10.1137/16M1082469](https://doi.org/10.1137/16M1082469).
- [52] Gabriel Peyré and Marco Cuturi. Computational optimal transport: With applications to data science. *Foundations and Trends in Machine Learning*, 11(5–6):355–607, 2019. doi:[10.1561/22000000073](https://doi.org/10.1561/22000000073).
- [53] Federico Pichi, Maria Strazzullo, Francesco Ballarin, and Gianluigi Rozza. Driving bifurcating parametrized nonlinear PDEs by optimal control strategies: Application to Navier–Stokes equations with model order reduction. *ESAIM: Mathematical Modelling and Numerical Analysis*, 56(4):1361–1400, 2022. doi:[10.1051/m2an/2022044](https://doi.org/10.1051/m2an/2022044).
- [54] Federico Pichi, Francesco Ballarin, Gianluigi Rozza, and Jan S. Hesthaven. An artificial neural network approach to bifurcating phenomena in computational fluid dynamics. *Computers & Fluids*, 254:105813, 2023. doi:[10.1016/j.compfluid.2023.105813](https://doi.org/10.1016/j.compfluid.2023.105813).
- [55] Federico Pichi, Beatriz Moya, and Jan S. Hesthaven. A graph convolutional autoencoder approach to model order reduction for parametrized PDEs. *Journal of Computational Physics*, 501:112762, 2024. doi:[10.1016/j.jcp.2024.112762](https://doi.org/10.1016/j.jcp.2024.112762).
- [56] Alfio Quarteroni and Alberto Valli. *Numerical Approximation of Partial Differential Equations*. Springer-Verlag, 1994.

- [57] Alfio Quarteroni, Andrea Manzoni, and Federico Negri. *Reduced Basis Methods for Partial Differential Equations*. UNITEXT. Springer International Publishing, 2016. doi:[10.1007/978-3-319-15431-2](https://doi.org/10.1007/978-3-319-15431-2).
- [58] William J Rider and Douglas B Kothe. Reconstructing volume tracking. *Journal of Computational Physics*, 141:112–152, 1998.
- [59] Donsub Rim, Benjamin Peherstorfer, and Kyle T. Mandli. Manifold approximations via transported subspaces: Model reduction for transport-dominated problems. *SIAM Journal on Scientific Computing*, 45(1):A170–A199, 2023. doi:[10.1137/20M1316998](https://doi.org/10.1137/20M1316998).
- [60] Alessio Roccon. Boiling heat transfer by phase-field method: A. roccon. *Acta Mechanica*, 236(9):5623–5638, 2025.
- [61] Alessio Roccon, Francesco Zonta, and Alfredo Soldati. Phase-field modeling of complex interface dynamics in drop-laden turbulence. *Physical Review Fluids*, 8(9):090501, 2023.
- [62] Francesco Romor, Federico Pichi, Giovanni Stabile, Gianluigi Rozza, and Christoph Schwab. ROM for Viscous, Incompressible Flow in Polygons – exponential n-width bounds and convergence rate. 2025. doi:[10.48550/arXiv.2512.22567](https://doi.org/10.48550/arXiv.2512.22567).
- [63] Salar Zamani Salimi, Aritra Mukherjee, Marica Pelanti, and Luca Brandt. A low mach number diffuse-interface model for multicomponent two-phase flows with phase change. *Journal of Computational Physics*, 523:113683, 2025.
- [64] Filippo Santambrogio. *Optimal Transport for Applied Mathematicians: Calculus of Variations, PDEs, and Modeling*, volume 87 of *Progress in Nonlinear Differential Equations and Their Applications*. Springer International Publishing, Cham, 2015. ISBN 978-3-319-20827-5 978-3-319-20828-2. doi:[10.1007/978-3-319-20828-2](https://doi.org/10.1007/978-3-319-20828-2).
- [65] Richard Saurel and Carlos Pantano. Diffuse-interface capturing methods for compressible two-phase flows. *Annual Review of Fluid Mechanics*, 50:105–130, 2018.
- [66] Bernhard Schmitzer. Stabilized sparse scaling algorithms for entropy regularized transport problems. *SIAM Journal on Scientific Computing*, 41(3):A1443–A1481, 2019. doi:[10.1137/16m1106018](https://doi.org/10.1137/16m1106018).
- [67] Lawrence Sirovich. Turbulence and the Dynamics of Coherent Structures Part I: Coherent Structures. *Quarterly of Applied Mathematics*, 45(3):561–571, 1987.
- [68] Giovanni Soligo, Alessio Roccon, and Alfredo Soldati. Breakage, coalescence and size distribution of surfactant-laden droplets in turbulent flow. *Journal of Fluid Mechanics*, 881:244–282, 2019.
- [69] Giovanni Soligo, Alessio Roccon, and Alfredo Soldati. Mass-conservation-improved phase field methods for turbulent multiphase flow simulation: G. soligo et al. *Acta Mechanica*, 230(2):683–696, 2019.
- [70] Tommaso Taddei. A registration method for model order reduction: Data compression and geometry reduction. *SIAM Journal on Scientific Computing*, 42(2):A997–A1027, 2020. doi:[10.1137/19M1271270](https://doi.org/10.1137/19M1271270).
- [71] Niccolò Tonicello and Matthias Ihme. A high-order diffused-interface approach for two-phase compressible flow simulations using a discontinuous galerkin framework. *Journal of Computational Physics*, 508:112983, 2024.
- [72] Niccolò Tonicello, Guido Lodato, and Matthias Ihme. Extension of a spectral difference method for the diffused-interface five-equation model. *Computers & Fluids*, page 106880, 2025.
- [73] C. Villani. *Topics in Optimal Transportation*. Graduate Studies in Mathematics. American Mathematical Society, 2021.
- [74] Lorenz Weber, Aritra Mukherjee, Andreas G Class, and Luca Brandt. A consistent and scalable framework suitable for boiling flows using the conservative diffuse interface method. *Journal of Computational Physics*, page 114680, 2026.